

## ROBUSTNESS OF COSMOLOGICAL SIMULATIONS I: LARGE SCALE STRUCTURE

KATRIN HEITMANN<sup>1</sup>, PAUL M. RICKER<sup>2,3</sup>, MICHAEL S. WARREN<sup>4</sup>, AND SALMAN HABIB<sup>5</sup><sup>1</sup> ISR-1, ISR Division, The University of California, Los Alamos National Laboratory, Los Alamos, NM 87545<sup>2</sup> Dept. of Astronomy, University of Illinois, Urbana, IL 61801<sup>3</sup> National Center for Supercomputing Applications, Urbana, IL 61801<sup>4</sup> T-6, Theoretical Division, The University of California, Los Alamos National Laboratory, Los Alamos, NM 87545<sup>5</sup> T-8, Theoretical Division, The University of California, Los Alamos National Laboratory, Los Alamos, NM 87545*Draft version October 31, 2018*

## ABSTRACT

The gravitationally-driven evolution of cold dark matter dominates the formation of structure in the Universe over a wide range of length scales. While the longest scales can be treated by perturbation theory, a fully quantitative understanding of nonlinear effects requires the application of large-scale particle simulation methods. Additionally, precision predictions for next-generation observations, such as weak gravitational lensing, can only be obtained from numerical simulations. In this paper, we compare results from several N-body codes using test problems and a diverse set of diagnostics, focusing on a medium resolution regime appropriate for studying many observationally relevant aspects of structure formation. Our conclusions are that, despite the use of different algorithms and error-control methodologies, with a few exceptions, the codes give very consistent results. Typically, the agreement over a wide range of scales is at the 5% level or better. The simulation results, including halo catalogs, and initial conditions used, are publicly available.

*Subject headings:* methods: N-body simulations — cosmology: large-scale structure of the universe

## 1. INTRODUCTION

1.1. *Motivation*

There is strong evidence that structure formation in the Universe is largely driven by gravitational instability. In the cosmological ‘standard model’ the evolution and structure of the mass distribution is supposed to be dominated by ‘dark matter,’ an as yet undetected type of matter that interacts only gravitationally. In order to study spatial and temporal aspects of the mass distribution today, it is convenient to consider three length scales: very large length scales where a linear treatment of the instability suffices, an intermediate length scale where nonlinearities cannot be neglected yet the dynamics of baryons are not of significant importance, and a high-resolution regime where gas dynamics, star formation, etc. need to be taken into account. While an analytic treatment is adequate at the largest scales, because of the nonlinearity, both the intermediate and small-scale regimes require a numerical approach.

In cold dark matter-dominated cosmologies, the transition from the linear regime to the nonlinear regime at  $z = 0$  occurs at length scales of order several  $h^{-1}$  Mpc (or  $k \sim 0.1$   $h\text{Mpc}^{-1}$ ). Depending on the application, length scales larger than this can often be satisfactorily treated by linear theory, augmented by perturbative corrections as needed. Galaxies exist within dark matter halos, and typical halo size scales are  $\sim 0.1 - 1$  Mpc. Thus, in order to resolve the dynamics of halos, a spatial resolution  $\sim 10$  kpc appears to be necessary. (Here we will not be interested in questions relating to the cores of halos and halo substructure, where even higher resolution is needed.)

This is the first of two papers where we carry out comparison studies of cosmological simulations focusing only on the dynamics of cold dark matter. Given the dominance of this component in the matter budget and expected precision observations of the matter distribution from large scale structure and lensing studies, however, we believe these studies to be timely and important. Realistic simulations of clusters and galaxy forma-

tion require high-resolution treatments of both dark matter and gas dynamics including feedback from star formation, AGNs, gas preheating, etc. There is not yet complete agreement on how all of these effects should be incorporated; therefore, we believe that it is too early to attempt a more complete study.

In this paper, we focus on medium resolution simulations, i.e., where the spatial resolution is  $\sim 10 - 100$  kpc. These simulations are adequate for matter power spectrum computations, for weak lensing studies, and for gathering cluster statistics. In the next paper, we will focus on higher-resolution simulations which aim to resolve individual galactic halos.

The main purpose of this work is to characterize the variation of results from different cosmological simulation codes, all codes being given exactly the same initial conditions, and all results being analyzed in identical fashion. The point of the tests carried out in this paper is to identify systematic differences between code results and, to the extent possible, attempt to identify the reasons behind gross discrepancies, should such arise. The aim is not to tune the codes to agree within some pre-defined error but rather to explore the variability in the results when the codes are run using “reasonable” simulation parameters. In addition, it is also not our purpose to establish which code is “best” for which application; while we have often run codes with different force resolutions to illustrate general points, we have made no effort to carry out a detailed benchmarking exercise. Finally, the characterization of intrinsically statistical issues such as limitations arising from finite sampling and studies of the physical/observational relevance of the diagnostic tools employed (e.g., halo finders) lie beyond the scope of this paper.

1.2. *N-body Simulation*

At the scales of interest to structure formation a Newtonian approximation is sufficient to describe gravitational dynamics (Peebles 1980). The task is therefore reduced to solving a (collisionless) Vlasov-Poisson equation. This equation is

a six-dimensional partial differential equation, thus, on memory grounds alone, a brute force approach cannot be applied. In addition, because of its essential nonlinearity, the Vlasov-Poisson equation generates ever-smaller spatial structures with time; it therefore becomes necessary to utilize a robust scheme that avoids instabilities as structure is created on sub-resolution scales. Having first made their appearance in plasma physics, N-body codes form a now-standard approach for dealing with this problem (Klypin & Shandarin 1983, Efstathiou et al. 1985, Sellwood 1987, Hockney & Eastwood 1989, Birdsall & Langdon 1991, Bertschinger 1998, Couchman 1999).

In the N-body approach, the six-dimensional phase space distribution is sampled by ‘tracer’ particles and these particles are evolved by computing the inter-particle gravitational forces. Since for  $N$  particles this is a computationally intensive  $O(N^2)$  problem, approximation techniques are used to reduce the force computation to  $\sim O(N)$  or  $\sim O(N \log N)$ . These approximation techniques are typically grid-based or employ multipole expansions, or are hybrids of the two. Finally, the addition of gas dynamics is accomplished by coupling the N-body solver to a hydro-code (other effects such as star-formation, etc. can be treated by employing sub-grid techniques).

As stated above, the purpose of this paper is to investigate the consistency of results from purely gravitational N-body codes in the moderate resolution regime. (While performance issues are also important, they will not be considered here.) In this regime, planned observations are now reaching the point where it is necessary that simulations be performed to low single-digit (percentage) accuracy (Refregier et al. 2004). To establish an initial baseline, we systematically compare results from the following codes: MC<sup>2</sup> (Mesh-based Cosmology Code) (Habib et al. 2004), a direct parallel particle-mesh (PM) solver; FLASH (Fryxell et al. 2000), an adaptive-mesh-refinement (AMR) grid code; HOT (Hashed-Oct Tree) (Warren & Salmon 1993), a tree-code; the tree code GADGET (GAlaxies with Dark matter and Gas intEraCtions) (Springel et al. 2001); HYDRA, an adaptive-mesh P<sup>3</sup>M-SPH code (Couchman et al. 1995), and TPM, a tree particle mesh code (Xu 1995 and Bode et al. 2000). FLASH, GADGET, HYDRA, and TPM are publicly available.

A variety of tests and diagnostic tools have been employed; in all cases, the codes were run with identical initial conditions and the results analyzed with identical diagnostic tools. We begin with the Zel’dovich pancake collapse test to investigate issues of convergence and collisionality (Melott et al. 1997). We then turn to two relatively realistic situations, the Santa Barbara cluster comparison (Frenk et al. 1999) and ‘concordance’  $\Lambda$ CDM simulations. Several diagnostics such as velocity statistics, halo catalogs, mass functions, correlation functions and power spectra, etc. were used to compare code results. The initial conditions, outputs from all codes at  $z = 0$ , and halo catalogs used in this paper are publicly available<sup>1</sup>.

The organization of the paper is as follows. In Sec. 2, we give a short general introduction to N-body methods, followed by summaries of the six different codes employed here. In Sec. 3 we discuss results from the Zel’dovich pancake test, focusing on questions regarding symmetry-breaking and collisionality. In Secs. 4 and 5, we describe results from the Santa Barbara cluster test and simulations based on the parameters for the cosmological Standard Model as measured by WMAP (Spergel et al. 2003) and other observations. In Sec. 6 we discuss our re-

sults for the different codes and summarize our conclusions.

## 2. THE N-BODY PROBLEM FOR DARK MATTER

The Vlasov-Poisson equation in an expanding Universe describes the evolution of the six-dimensional, one-particle distribution function,  $f(\mathbf{x}, \mathbf{p})$  (Vlasov equation):

$$\frac{\partial f(\mathbf{x}, \mathbf{p})}{\partial t} = -\frac{\mathbf{p}}{ma^2} \cdot \nabla f(\mathbf{x}, \mathbf{p}) + m \nabla \Phi(\mathbf{x}) \cdot \frac{\partial f(\mathbf{x}, \mathbf{p})}{\partial \mathbf{p}}, \quad (1)$$

where  $\mathbf{x}$  is the comoving coordinate,  $\mathbf{p} = ma^2 \dot{\mathbf{x}}$ ,  $m$ , the particle mass, and  $\Phi(\mathbf{x})$ , the self-consistent gravitational potential, determined by solving the Poisson equation,

$$\nabla^2 \Phi(\mathbf{x}) = 4\pi G a^2 [\rho(\mathbf{x}, t) - \rho_b(t)], \quad (2)$$

where  $\rho_b$  is the background mass density and  $G$  is the Newtonian constant of gravitation. The Vlasov-Poisson system, Eqns. (1) – (2) constitutes a collisionless, mean-field approximation to the evolution of the full N-particle distribution. As mentioned earlier, N-body codes attempt to solve Eqns. (1) – (2), by representing the one-particle distribution function as

$$f(\mathbf{x}, \mathbf{p}) = \sum_{i=1}^N \delta(\mathbf{x} - \mathbf{x}_i) \delta(\mathbf{p} - \mathbf{p}_i). \quad (3)$$

Substitution of Eqn. (3) in the Vlasov-Poisson system of equations yields the exact Newton’s equations for a system of  $N$  gravitating particles. It is important to keep in mind, however, that we are not really interested in solving the exact N-body problem for a finite number of particles,  $N$ . The actual problem of interest is the exact N-body problem in the fluid limit, i.e., as  $N \rightarrow \infty$ . For this reason, one important aspect of the numerical fidelity of N-body codes lies in controlling errors due to the discrete nature of the particle representation of  $f(\mathbf{x}, \mathbf{p})$ . Once the representation (3) is accepted, errors also arise from time-stepping of the Newton’s equations as well as in solving the Poisson equation (2). While heuristic prescriptions are routinely followed and tested (see, e.g., Power et al. 2003), a comprehensive theory of N-body errors does not yet exist.

Determining the forces for  $N$  particles exactly requires  $O(N^2)$  calculations. This is an unacceptable computational cost at the large values of  $N$  typical in modern N-body codes ( $N \geq 10^7$ ), especially as we are not interested in the exact solution in the first place. Two popular approximate methods are used to get around this problem – the first introduces a spatial grid and the second employs a multipole expansion. Hybrid algorithms that meld grid and particle-force calculations are also common. The simplest  $O(N \log N)$  grid code uses a particle-mesh (PM) methodology wherein the particle positions are sampled to yield a density field  $\rho(\mathbf{x})$  on a regular grid. The Poisson equation is then solved by Fourier or other (e.g., multi-grid) methods, and the force interpolated back on the particles. Improvement on the grid resolution can be achieved by adaptive mesh refinement (AMR) and by direct particle force computation for particles within a few grid cells – the particle-particle particle mesh (P<sup>3</sup>M) method. Tree codes are based on the idea of approximating the gravitational potential of a set of particles by a multipole expansion. All the particles are arranged in a hierarchical group structure with the topology of a tree. Given a point at which the potential needs to be evaluated and a particular particle group, one decides if the point is sufficiently far away (opening angle criterion) in order for a (suitably truncated) multipole expansion to be used; if not, the subgroups of the parent group are investigated. The process is continued until all groups are fully searched down to the individual particle level.

<sup>1</sup><http://18web.lanl.gov/people/heitmann/arxiv/>

Basic grid methods such as PM are fast, relatively simple to implement, and memory-efficient. Consequently, they have good mass resolution, but due to the limited dynamic range of the three-dimensional spatial grid, only moderate force resolution. Tree codes are gridless and have much better force resolution, but this typically involves a performance and memory cost. Adaptive mesh and hybrid algorithms such as tree-PM (TPM) constitute further steps in attaining better compromises between mass and force resolution. (Due to discreteness/collisionality errors, excellent force resolution with poor mass resolution is potentially just as problematic as the reverse.)

### 2.1. The Codes

The codes utilized in this study have different algorithms, possess different error modes and employ different error control strategies. Thus, good convergence to a single solution is a strong test of the validity of the N-body approach in modeling dissipationless gravitational dynamics at the resolution scales probed by the tests. We emphasize that the codes were run with no special effort to optimize parameters separately for the individual test problems; to conform to typical usage, only the recommended default parameter values were used. Separate introductions to the codes are given below.

#### 2.1.1. $MC^2$

The multi-species  $MC^2$  code suite (Habib et al. 2004) includes a parallel PM solver for application to large scale structure formation problems in cosmology. In part, the code descended from parallel space-charge solvers for studying high-current charged-particle beams developed at Los Alamos National Laboratory under a DOE Grand Challenge (Ryne et al. 1998, Qiang et al. 2000). It exists in two versions: a simpler version meant for fast prototyping and algorithm development written in High Performance Fortran (HPF), and a high-performance version based on Viktor Decyk's F90/MPI UPIC framework (Decyk and Norton). This code has excellent mass resolution and has proven its efficiency on multiple HPC platforms, with scaling being verified up to 2000 processors.

$MC^2$  solves the Vlasov-Poisson system of equations for an expanding universe using standard mass deposition and force interpolation methods allowing for periodic or open boundary conditions with second and fourth-order (global) symplectic time-stepping and a Fast Fourier Transform (FFT)-based Poisson solver. The results reported in this paper were obtained using Cloud-In-Cell (CIC) deposition/interpolation. The overall computational scheme has proven to be remarkably accurate and efficient: relatively large time-steps are possible with exceptional energy conservation being achieved.

#### 2.1.2. FLASH

FLASH (Fryxell et al. 2000) originated as an AMR hydrodynamics code designed to study X-ray bursts, novae, and Type Ia supernovae as part of the DOE ASCI Alliances Program. Block-structured adaptive mesh refinement is provided via the PARAMESH library (MacNeice et al. 2000). FLASH uses an oct-tree refinement scheme similar to Quirk (1991) and de Zeeuw and Powell (1993). Each mesh block contains the same number of zones ( $16^3$  for the runs in this paper), and its neighbors must be at the same level of refinement or one level higher or lower (mesh consistency criterion). Adjacent refinement levels are separated by a factor of two in spatial resolution. The refinement criterion used is based upon logarithmic density

thresholds. The mesh is fully refined to the level at which the initial conditions contain one particle per zone. Blocks with maximum densities between 30 and 300 times the average are refined by one additional level. Those with maxima between 300 and 3000 times the average are refined by two additional levels, and each factor of 10 in maximum density above that corresponds to an additional level of refinement. FLASH has been extensively verified and validated, is scalable to thousands of processors, and extensible to new problems (Rosner et al. 2000, Calder et al. 2000, and Calder et al. 2002).

Numerous extensions to FLASH have been developed, including solvers for thermal conduction, magnetohydrodynamics, radiative cooling, self-gravity, and particle dynamics. In particular, FLASH now includes a multigrid solver for self-gravity and an adaptive particle-mesh solver for particle dynamics (Ricker et al. 2004). Together with the PPM hydrodynamics module, these provide the core of FLASH's cosmological simulation capabilities. FLASH uses a variable-timestep leapfrog integrator. In addition to other timestep limiters, the FLASH particle module requires that particles travel no more than a fraction of a zone during a timestep.

#### 2.1.3. HOT

This parallel tree code (Warren & Salmon 1993) has been evolving for over a decade on many platforms. The basic algorithm may be divided into several stages (the method of error tolerance is described in Salmon & Warren 1994). First, particles are domain decomposed into spatial groups. Second, a distributed tree data structure is constructed. In the main stage of the algorithm, this tree is traversed independently in each processor, with requests for non-local data being generated as needed. A Key is assigned to each particle, which is based on Morton ordering. This maps the points in 3-dimensional space to a 1-dimensional list, maintaining as much spatial locality as possible. The domain decomposition is obtained by splitting this list into  $N_p$  (number of processors) pieces. An efficient mechanism for latency hiding in the tree traversal phase of the algorithm is critical. To avoid stalls during non-local data access, effectively explicit 'context switching' is done using a software queue to keep track of which computations have been put aside waiting for messages to arrive. This code architecture allows HOT to perform efficiently on parallel machines with fairly high communication latencies (Warren et al. 2003). This code was among the ones used for the original Santa Barbara Cluster Comparison Project (Frenk et al. 1999) and also supports gas dynamics simulations via a smoothed particle hydrodynamics (SPH) module (Fryer & Warren 2002).

#### 2.1.4. GADGET

GADGET (Springel et al. 2001) is a freely available N-body/hydro code capable of operating both in serial and parallel modes. For the tests performed in this paper the parallel version was used. The gravitational solver is based on a hierarchical tree-algorithm while the gas dynamics (not used here) are evolved by SPH. GADGET allows for open and periodic boundary conditions, the latter implemented via an Ewald summation technique. The code uses individual and adaptive time steps for all particles.

#### 2.1.5. HYDRA

HYDRA (Couchman et al. 1995) is an adaptive  $P^3M$  ( $AP^3M$ ) code with additional SPH capability. In this paper we use HYDRA only in the collisionless mode by switching off the gas

dynamics. The  $P^3M$  method combines mesh force calculations with direct summation of inter-particle forces on scales of two to three grid spacings. In regions of strong clustering, the direct force calculations can become significantly expensive. In  $AP^3M$ , this problem is tackled by utilizing multiple levels of subgrids in these high density regions, with direct force computations carried out on two to three spacings of the higher-resolution meshes. Two different boundary conditions are implemented in HYDRA, periodic and isolated. The timestep algorithm in the dark matter-only mode is equivalent to a leapfrog algorithm.

### 2.1.6. TPM

TPM (Xu 1995 and Bode et al. 2000), a tree particle-mesh N-body algorithm, is a hybrid code combining a PM and a tree algorithm. The density field is broken down into many isolated high-density regions which contain most of the mass in the simulation but only a small fraction of the volume. In these regions the gravitational forces are computed with the tree algorithm while for the bulk of the volume the forces are calculated via a PM algorithm, the PM time steps being large compared to the time-steps for the tree-algorithm. The time integrator in TPM is a standard leap-frog scheme: the PM timesteps are fixed whereas the timesteps for the tree-particles are variable.

## 3. THE ZEL'DOVICH PANCAKE TEST

### 3.1. Description of Test

The cosmological pancake problem (Zel'dovich 1970, Shandarin & Zeldovich 1989) provides a good simultaneous test of particle dynamics, Poisson solver, and cosmological expansion. Analytic solutions well into the nonlinear regime are available for both dark matter and hydrodynamical codes (Anninos & Norman 1994), permitting an assessment of code accuracy. After caustic formation, where the analytic results fail, the problem continues to provide a stringent test of the ability to track thin, poorly resolved features (Melott 1983).

As is conventional, we set the initial conditions for the pancake problem in the linear regime. In a universe with  $\Omega_0 = 1$  at redshift  $z$ , a perturbation of wavenumber  $k$  which collapses to a caustic at redshift  $z_c < z$  has comoving density and velocity given by

$$\rho(x_e; z) = \bar{\rho} \left[ 1 - \frac{1+z_c}{1+z} \cos(kx_\ell) \right]^{-1}, \quad (4)$$

$$v(x_e; z) = -H_0(1+z)^{1/2}(1+z_c) \frac{\sin kx_\ell}{kx_\ell}, \quad (5)$$

where  $\bar{\rho}$  is the comoving mean density. Here  $x_e$  is the distance of a point from the pancake midplane, and  $x_\ell$  is the corresponding Lagrangian coordinate, found by iteratively solving

$$x_e = x_\ell - \frac{1+z_c}{1+z} \frac{\sin kx_\ell}{k}. \quad (6)$$

The Lagrangian coordinates for the dark matter particles  $x_\ell$  are assigned to lie on a uniform grid. The corresponding perturbed coordinates  $x_e$  are computed using Eqn. (6). Particle velocities are assigned using Eqn. (5).

As particles accelerate toward the midplane, their phase profile develops a backwards “S” shape. At caustic formation the velocity becomes multivalued at the midplane. The region containing multiple streams grows in size as particles pass through the midplane. At the edges of this region (the caustics, or the

inflection points of the “S”), the particle density is formally infinite, although the finite force and mass resolution in the simulations keeps the height of these peaks finite. Some of the particles that have passed through the midplane fall back and form another pair of caustics, twisting the phase profile again. Because each of these secondary caustics contains five streams of particles rather than three, the second pair of density peaks are higher than the first pair. In principle, this caustic formation process repeats arbitrarily many times. In practice, however, the finite number of particles and the finite force resolution in simulations limit the number of caustics that can be tracked.

In Melott et al. (1997) the pancake simulation was used to test different codes for unphysical collisionality and symmetry-breaking. It was found that tree and  $P^3M$  codes suffered from artifacts if the value of the softening parameter was chosen too small, leading to incorrect results for the pancake test. We have carried out a set of simulations to distinguish between lack of convergence due to collisional effects and the failure of the test due to the inability to strictly track the planar symmetry of the mass distribution. Our basic conclusions are that for the mass and force resolutions chosen in the main cosmological simulations in this paper, collisional effects are unlikely to be important. While it is true that the high-resolution codes fail at maintaining the symmetry of the pancake test, the PM-code  $MC^2$  does not. Thus, one may verify whether this failure is an issue in realistic simulations by comparing results for the different codes, as we do later in the paper. Our results are consistent with the finding that, at least in the moderate resolution regime, this failure in the pancake test does not translate to making significant errors in more realistic simulations.

### 3.1.1. Pancake Simulations

Our main aim in performing the pancake simulations is to probe whether the codes are working correctly in the dynamical range of interest. For this purpose, small simulations are sufficient; what is important is to match the mass resolution and the spatial resolution to the ones used in the larger cosmological simulations. Most of these larger simulations used  $256^3$  particles, the box sizes varying between 64 Mpc, 90 Mpc, and 360 Mpc, with different cosmologies. This leads to particle masses of  $1.08 \cdot 10^9 M_\odot$ ,  $1.9 \cdot 10^9 M_\odot$ , and  $1.22 \cdot 10^{11} M_\odot$ . We perform the pancake test in a  $\sqrt{3} \cdot 10$  Mpc box, with  $64^3$  particles. This leads to a particle mass of  $1.4 \cdot 10^9 M_\odot$ , which provides a good representation for the cosmological test problems. In order to almost match the force resolution of the PM code with the other codes we ran it using a  $1024^3$  grid in the cosmological simulations. For the 64 Mpc and 90 Mpc boxes, this is approximately equivalent to running the pancake test with a  $256^3$  PM grid.

Based on these considerations, the following simulations were run: for the cosmology we chose a SCDM model, i.e.  $\Omega_m = 1$ ,  $H = 50$  km/s/Mpc,  $\Omega_b = \Omega_\Lambda = 0$ , in a  $\sqrt{3} \cdot 10$  Mpc box with  $64^3$  particles in all cases. HOT was run with a (Plummer) smoothing of 20 kpc while the smoothing for the HYDRA-simulation was chosen to be 100 kpc. In AMR mode, the FLASH grid size was refined up to three times, leading up to an effective  $512^3$  grid. We varied the mesh size for the  $MC^2$  simulation between  $64^3$  and  $512^3$  to check convergence for increasing number of grid points. The TPM and GADGET runs did not complete successfully for this test.

The initial conditions are set up such that the pancake normal is aligned with the box diagonal, i.e., inclined at 54.7 degrees with respect to the base plane. In order to check our results

we performed a high-resolution one-dimensional pancake simulation to serve as a comparison template. Due to the lack of an analytical solution, this numerical comparison is important for verifying our results in the nonlinear regime, after several caustics have formed.

### 3.1.2. Results

The initial conditions were chosen so that the redshift at which the first collapse occurs is  $z_c = 5$ . We measured the positions and velocities of the particles at  $z = 7$ , i.e., before the collapse, and also at  $z = 0$  after several caustics have formed. The results are displayed in phase-space plots, where positions and velocities are projected onto the box diagonal.

At  $z = 7$ , before caustic formation occurs, all codes perform very well as can be seen in Fig. 1. In addition, we performed a convergence test with the PM-code  $MC^2$ . We ran a  $64^3$  particle simulation on a mesh which was refined four times, from  $64^3$  to  $512^3$  mesh points (Fig. 1 shows the  $MC^2$  result from the  $256^3$  mesh). At  $z = 7$ , even the lowest resolution simulation with a  $64^3$  mesh, e.g., the analogous result for FLASH in Fig. 1), traces the exact solution accurately. Expectedly, increasing the number of mesh-points improves the result mainly near the region of maximal density variation, i.e., at  $x = 2.5$  Mpc. No failure of convergence was noted at the highest-resolution  $512^3$  simulation.

In contrast, by the time several caustics have formed, as shown in Fig. 2 for  $z = 0$ , the code results display considerable variation and lack of convergence. To understand this behavior, we first turn to a convergence test with  $MC^2$  shown in Fig. 3. Here we have zoomed into the inner part of the phase-space spiral by restricting the  $x$  axis between 2.3 and 2.7 Mpc. While the  $64^3$  mesh simulation can track the first two caustics, the inner part of the spiral is not resolved. A  $128^3$  mesh provides some improvement, while a  $256^3$  mesh – corresponding to a resolution of 67 kpc – leads to satisfactory agreement with the essentially exact 1-D numerical solution (in Fig. 2, the  $MC^2$  results are shown for the  $256^3$  mesh simulation). This is the level of  $MC^2$  spatial resolution used for the cosmological simulations.

As the mesh is refined further, collisional effects must enter at some point. In fact, by refining the grid one more time and running the  $64^3$  particles on a  $512^3$  mesh (corresponding to a resolution of 34 kpc) the failure of convergence can be directly observed. While the increase from a  $64^3$  mesh to a  $256^3$  mesh clearly led to a better refinement of the inner spiral, i.e. the simulation was converging towards the exact solution, a further increase of the spatial resolution does *not* continue the improvement. The particles on the inner part of the spiral are moving away from the exact solution instead of converging towards it. Collisional effects destroy the good convergence properties which were found for the smaller meshes. Therefore, small-scale resolved structures at this high level of spatial resolution can turn out to be incorrect. Convergence tests performed with FLASH with uniform resolution give similar results.

It is clear, however, that the results in Fig. 2 show artifacts much worse than the mild lack of convergence observed in Fig. 3. For example, the result from running FLASH with refinement turned on, yielding an effective  $512^3$  mesh, shows severe artifacts: the particle distribution is smeared out close to the center of the spiral. Note that the smearing seen here cannot be explained as a consequence of “over-resolution” as this effect is not seen in the  $MC^2$  results of Fig. 3, which have the same effective resolution. A similar result was obtained with

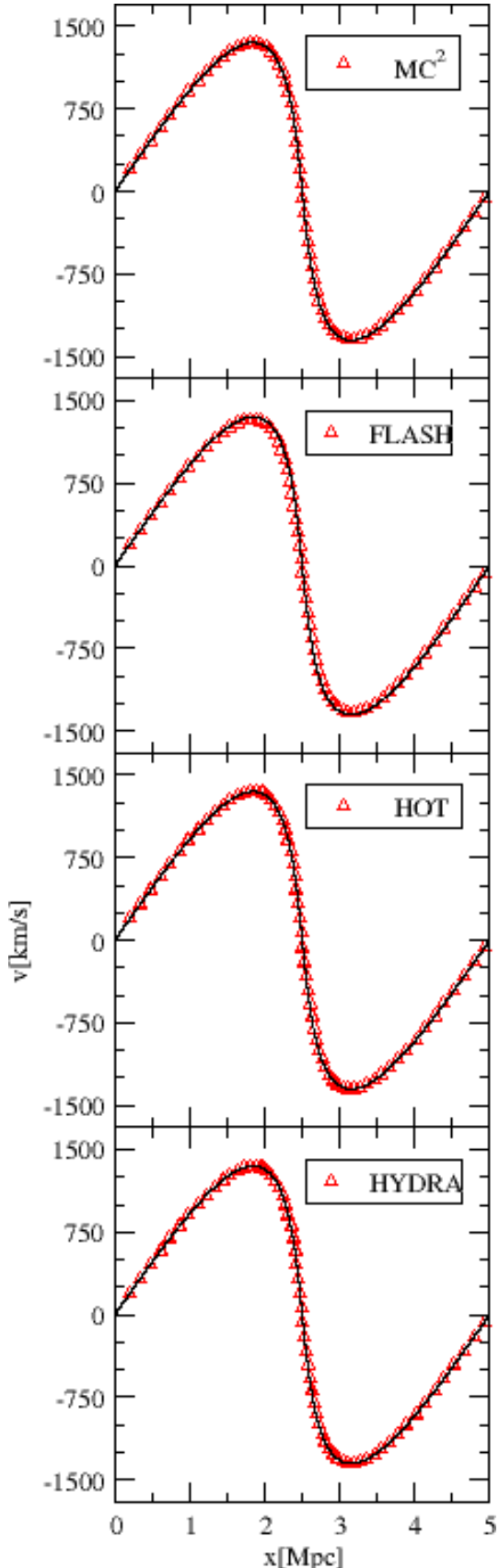


FIG. 1.— The phase plane for the pancake test from four simulations with  $64^3$  particles at  $z = 7$ , prior to caustic formation. As an illustration, the FLASH result is taken from a low-resolution  $64^3$  mesh to demonstrate the resulting small inaccuracies near the curve minimum and maximum. The solid lines are from a one-dimensional high-resolution simulation.

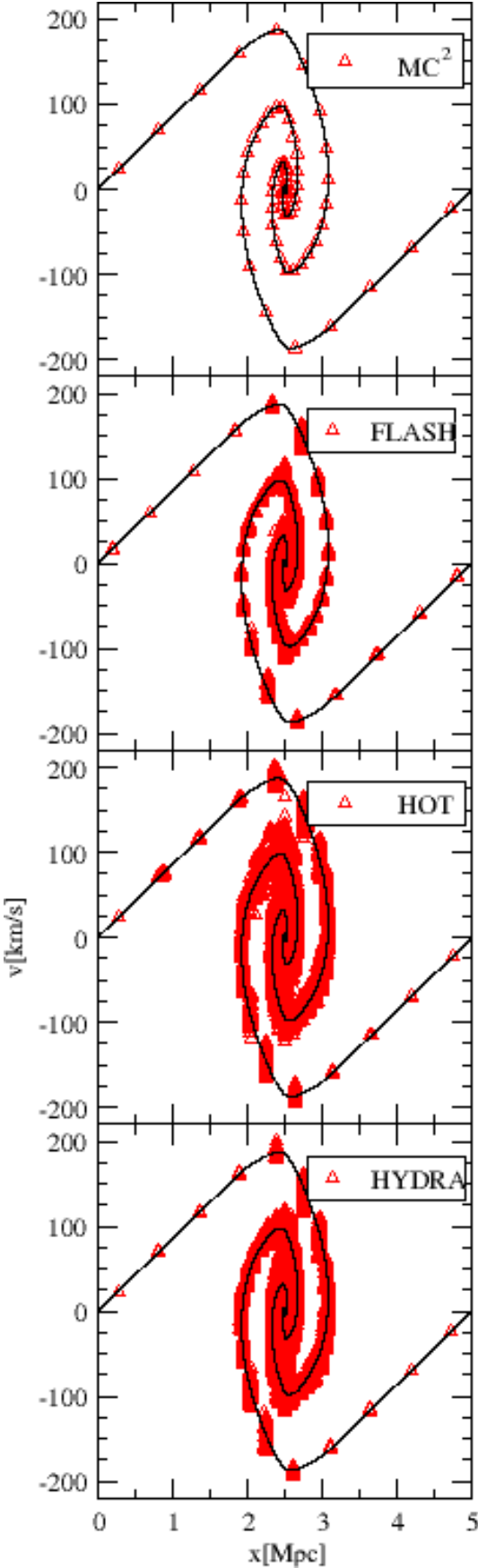


FIG. 2.— The pancake test at  $z = 0$ ,  $64^3$  particles, following Fig. 1. Very close to the origin, there is a seven-stream flow. Here, FLASH is run with an effective resolution equivalent to a  $512^3$  mesh. For a discussion of these results, see the text.

the tree-code HOT, where the structure of the inner spiral is more or less completely lost; the results from the AP<sup>3</sup>M code HYDRA are not any better. It is the failure of the AMR, tree, and AP<sup>3</sup>M codes to maintain the strict planar symmetry of the pancake collapse that is apparently the root cause of the problem. To reiterate, the  $256^3$  and  $512^3$  PM runs roughly span the force resolutions used for the other codes, and since only the  $512^3$  run shows a very mild failure of convergence, force resolution alone cannot be the source of the difficulty.

Our results provide a different and more optimistic interpretation of the findings of Melott et al. (1997). While high-resolution codes when run with small smoothing lengths (or several refinement levels in the case of AMR) are not able to pass the pancake test after the formation of several caustics, the main culprit appears to be an inability to maintain the planar symmetry of the problem and not direct collisionality (at least at the force resolutions relevant for this paper), which would have been far more serious. Whether the failure to treat planar collapse is a problem in more realistic situations can be tested by comparing results from the high-resolution codes against brute-force PM simulations. A battery of such tests have been carried out in Secs. 4 and 5. At the force resolutions investigated, these tests failed to yield evidence for significant deviations.

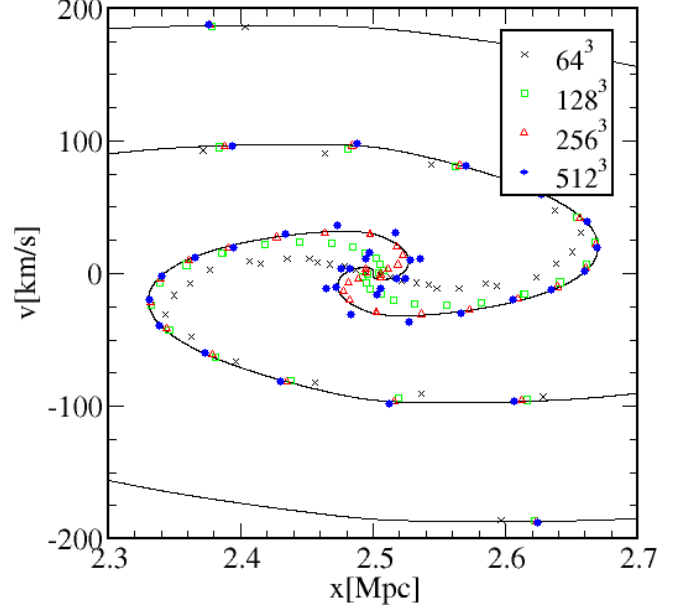


FIG. 3.— The failure of convergence near the midplane for the pancake test: MC<sup>2</sup> results,  $64^3$  particles with four grid sizes at  $z = 0$ . See the text for a discussion of these results.

#### 4. THE SANTA BARBARA CLUSTER

##### 4.1. Description of the Test

Results from the Santa Barbara Cluster Comparison Project were reported in 1999 in Frenk et al. (1999). The aim of this project was to compare different techniques for simulating the formation of a cluster of galaxies in a cold dark matter universe and to decide if the results from different codes were consistent and reproducible. For this purpose outputs from 12 different codes were examined, representing numerical techniques ranging from SPH to grid methods with fixed, deformable, and multilevel meshes. The starting point for every code was the same set of initial conditions given either by a set of initial po-

TABLE 1  
SOFTENING LENGTHS/MESH SPACING FOR THE SANTA BARBARA RUNS

	MC <sup>2</sup>	FLASH	HOT	GADGET	TPM	HYDRA
128 <sup>3</sup> particles	62.5 kpc	250 kpc	5 kpc (physical after z=9)	10 kpc	10 kpc	10 kpc
256 <sup>3</sup> particles	62.5 kpc	62.5 kpc	5 kpc (physical after z=9)	50 kpc	N/A	N/A

Note. — Resolutions of the different codes for the different Santa Barbara runs; the highest resolution runs were carried out with HOT. If not so noted, the resolution is quoted in comoving coordinates.

sitions or an initial density field. Every simulator was then allowed to evolve these initial conditions in a way best suited for the individual code, i.e., implementations of smoothing strategies, integration time steps, boundary conditions, etc. were not specified but their choice left to the individual simulators. The comparison was kept very general and practical; the main interest was not to quantify the accuracy of individual codes but to investigate the reliability of results from differing astrophysical simulations. For this purpose, images of clusters at different epochs were compared, as well as the mass, temperature, cluster luminosity, and radial profiles of various dynamical and thermodynamic quantities.

In this paper we restrict ourselves to the dark matter component of the simulation, run with periodic boundary conditions, and show results only at  $z = 0$ . In a departure from the original Santa Barbara project, we enforce strict uniformity by using the same particle initial condition for all the codes and using only one framework to analyze the final outputs of the simulations, e.g., the strategy of finding the center of the cluster is exactly the same for all simulations. This procedure allows for a uniform comparison of the different codes. In the following we briefly describe the simulations performed and then analyze and compare the individual results.

#### 4.2. Simulations Performed

The simulation of a single cluster in a small box is a time consuming task for most cosmology codes. The very high density region of the cluster demands very small time steps to resolve short orbital timescales. In order to avoid long run times, we therefore decided to run the original Santa Barbara test with 256<sup>3</sup> particles on only a subset of the tested codes: MC<sup>2</sup>, HOT, FLASH (our three main codes), and GADGET at a lower resolution than HOT. In addition we reduced the initial conditions from 256<sup>3</sup> particles to 128<sup>3</sup> particles by averaging over every eight particles and ran all six codes with these initial conditions. In this second set of simulations, lower-resolution FLASH results are used to convey some measure of sensitivity to resolution limits. The cosmology employed in the Santa Barbara test is SCDM, i.e.,  $\Omega_m = 1.0$  and the Hubble constant  $H = 50$  km/s/Mpc. The box size is 64 Mpc. The properties of the cluster were all measured at  $z = 0$ . Table 1 summarizes the resolutions at which the different simulations were performed.

#### 4.3. Results

As in the original Santa Barbara test paper (“SB paper” in the following) we study some specific properties of the cluster at  $z = 0$ , the velocity and density profiles, and projected images of the cluster itself.

We start our discussion with a useful but qualitative comparison, using images of the two-dimensional projected density of the cluster. All results are shown at  $z = 0$ . Figs. 4 and 5 display

the cluster in an 8 Mpc box from the 128<sup>3</sup> and the 256<sup>3</sup> simulations, respectively. In order to provide the best direct comparison we have not filtered the images. (A Gaussian smoothing of 250 kpc as used in the original paper washes out far too many details of the cluster which are real.) The density is projected onto a 1024<sup>2</sup>  $xy$ -plane grid and displayed in logarithmic units. The pixel size is 62.5 kpc which is substantially larger than the formal spatial resolution in the higher-resolution runs.

The overall appearance of the cluster – orientation, shape, size, highest density region in the center – agrees very well for all simulations. Comparing the 128<sup>3</sup> simulation from MC<sup>2</sup>, HOT, HYDRA, and TPM shows that many small scale features are reproduced with high fidelity. All four simulations show three small high density regions in the NE as well as three high density regions in the SW, and a high density region in the upper left corner of the plot. The FLASH image shows most of these features as well, but due to the lower resolution employed some of the very small features are missing – especially on the edge of the cluster. The GADGET results show some small deviations compared to the other simulations: The three high density regions in the NE visible in the other results reduce to two in the GADGET image, and the lower left corner doesn’t show as much structure. Overall one gets the impression that the GADGET image is not at  $z = 0$ , but slightly shifted. This may be due to a non-optimal setting of the maximum timestep in the GADGET configuration file (0.01). While this value is appropriate at low redshifts, in the linear regime GADGET will take timesteps equal in size to the MaxSizeTimestep parameter. We have not investigated whether making this parameter smaller would resolve this discrepancy. Sub-structure is clearly present in the HYDRA, HOT, and TPM images. However, there is a lack of one-to-one agreement at the level of these individual features.

The situation for the images from the 256<sup>3</sup> simulations shown in Fig. 5 is very similar. Due to better mass resolution the cluster appears to be smoother than in the 128<sup>3</sup> simulation. The agreement of the MC<sup>2</sup>, FLASH, and HOT results is excellent, as almost all obvious features (except the sub-structure) are identical. The HOT image shows more substructure than the MC<sup>2</sup> and FLASH images which is to be expected due to the higher force resolution of the tree-code compared to the mesh-codes. As in the 128<sup>3</sup>-particle simulation, the GADGET image seems to be taken at a slightly different redshift than the other ones. In summary the result of this qualitative comparison is very good – much better than in the original paper.

We continue with a more quantitative comparison of cluster properties. In Table 2 results for the radius  $r_{200}$  of the cluster measured in Mpc, the total mass measured in  $10^{15} M_\odot$ , and the rms velocity dispersion of the cluster in km/s are listed. We also give the average measurement for each quantity and the deviation from the average for the simulations.

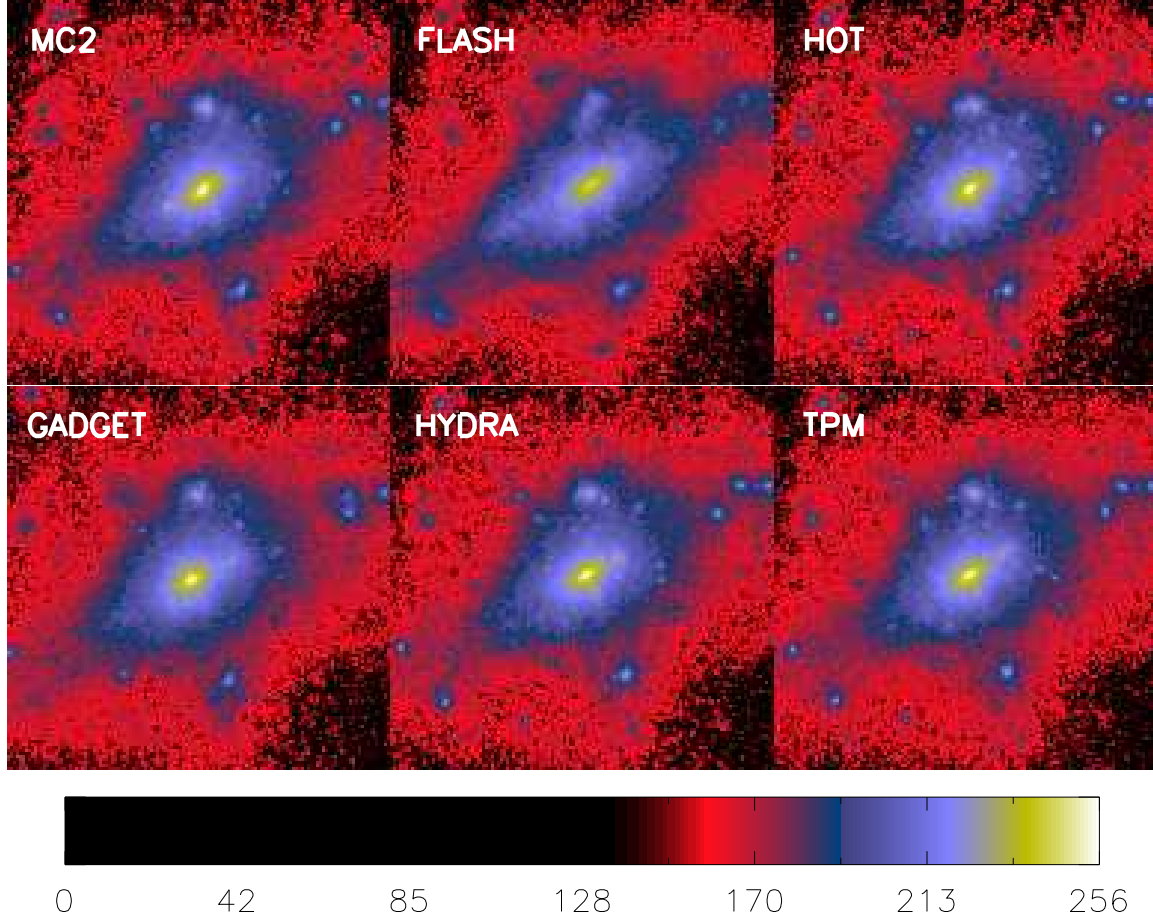


FIG. 4.— Santa Barbara cluster simulation: Projected dark matter density in logarithmic units at  $z = 0$ ,  $128^3$  particles projected on a  $1024^2$  mesh, no smoothing. The dynamic range of the density variation in this figure is roughly 5 orders of magnitude. The lower force resolution for the FLASH simulation is apparent in the figure.

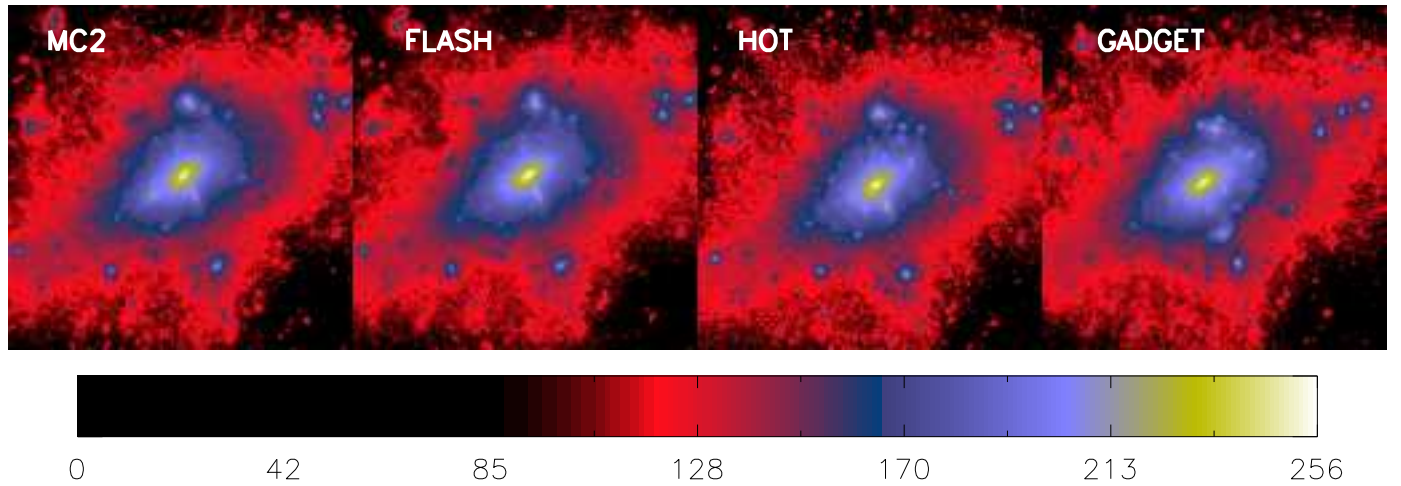


FIG. 5.— The projected dark matter density following Fig. 4, but for  $256^3$  particles. The FLASH force resolution is better by a factor of 4 than for the  $128^3$  particle run while the GADGET force resolution is 5 times worse. The force resolution for MC<sup>2</sup> and HOT are the same as in the  $128^3$  runs (see also Table 1). Note the increased definition of substructure independent of the force resolution.

TABLE 2  
CLUSTER PROPERTIES MEASURED AT  $z = 0$

	MC <sup>2</sup>	FLASH	HOT	GADGET	HYDRA	TPM	Average
<u><math>r_{200}</math> [Mpc]</u>							
128 <sup>3</sup>	2.753	2.753	2.753	2.753	2.753	2.753	2.753
Residual	—	—	—	—	—	—	—
256 <sup>3</sup>	2.753	2.753	2.753	2.753	N/A	N/A	2.753
Rel. Residual	—	—	—	—	N/A	N/A	N/A
<u><math>m_{\text{tot}}</math> [<math>10^{15} M_{\odot}</math>]</u>							
128 <sup>3</sup>	1.215	1.196	1.220	1.214	1.218	1.212	1.213
Rel. Residual	0.002	-0.01	0.006	0.001	0.005	0.0004	—
256 <sup>3</sup>	1.208	1.208	1.215	1.246	N/A	N/A	1.220
Rel. Residual	-0.01	-0.01	-0.004	0.02	N/A	N/A	N/A
<u><math>\sigma_{\text{DM}}</math> [km/s]</u>							
128 <sup>3</sup>	989.72	900.93	988.15	1009.66	1011.77	1007.03	984.54
Rel. Residual	0.005	-0.08	0.004	0.026	0.028	0.023	—
256 <sup>3</sup>	998.09	1016.79	1005.62	1012.05	N/A	N/A	1008.14
Rel. Residual	-0.01	0.009	-0.003	0.004	N/A	N/A	N/A

Independent of the number of particles ( $128^3$  or  $256^3$ ) all codes lead to exactly the same result for the radius of the cluster  $r_{200} = 2.753$  Mpc, which is slightly larger than the result from the original test,  $r_{200} = 2.70$  Mpc with an rms scatter of 0.04 Mpc.

The average mass for the cluster is  $1.21 \cdot 10^{15} M_{\odot}$  for the  $128^3$  particle simulation and  $1.22 \cdot 10^{15} M_{\odot}$  for the  $256^3$  simulation. This is a little higher than the average mass found in the original test; the highest mass reported from two runs in the SB paper was  $1.21 \cdot 10^{15} M_{\odot}$ . The deviation from the average for all runs is of the order of 1%, for some codes even sub-1%. Here we quote the relative residual calculated as  $(\langle x \rangle - \bar{x})/\langle x \rangle$ ,  $\langle x \rangle$  being the average of all results. In the original paper the agreement was reported to be sub-10%, an order of magnitude worse than our result. For the radius, the results from all the runs agree to three significant figures so no residuals are shown.

The average of the velocity dispersion  $\sigma_{\text{DM}}$  (following the convention of the original paper, the one-dimensional velocity dispersion  $\sigma_{\text{DM}} = \sigma/\sqrt{3}$  with  $\sigma$  being the three-dimensional velocity dispersion) is around 1000 km/s, slightly higher than in the SB paper. The agreement is remarkably good for both  $128^3$  and  $256^3$  particle simulations with a deviation of only around 1%. Due to the resolution limits, the  $128^3$ -FLASH simulation produces a value 8% lower than the average. In the original paper the differences in the individual code results were again much less satisfactory than in our comparison, with deviations of up to 10%. We discuss the reasons for the improved results later below.

Finally, we compare three different cluster profiles: the dark matter density, velocity dispersion, and the radial velocity as

functions of radius. These profiles were obtained by first determining the center of the cluster, and then averaging the particle information in 15 spherical shells evenly spaced in log radius. While we have shown all results for all codes down to the smallest radius, the results from MC<sup>2</sup>, FLASH, and GADGET for the  $256^3$  particle runs can be only trusted down to  $r = 0.06$  Mpc because of the resolution employed. For the  $128^3$  particle runs the force resolution of HOT, GADGET, HYDRA, and TPM is sufficient to generate correct results over the entire measured  $r$ -range while for MC<sup>2</sup> resolution artifacts are expected to be seen at  $r < 0.06$  Mpc and for FLASH at  $r < 0.2$  Mpc. Following the original SB paper, the main plots are in the lower panel with the average over the code results shown with a solid curve (we have removed the FLASH results from the average in the  $128^3$  particle simulations). In the upper panel the residuals are displayed, calculated as  $\ln x - \ln \langle x \rangle$  for the dark matter density and velocity dispersion profiles and  $x - \langle x \rangle$  for radial velocity profiles.

The dark matter density profile for the  $128^3$  particle runs is shown in Fig. 6. Down to a radius of  $r = 0.25$  Mpc the agreement of all codes is very good, at the sub-10% level. For smaller radii the FLASH profile falls off faster due to resolution limitations. The residuals for FLASH in the region  $r < 0.1$  Mpc are not shown. The agreement of the remaining five codes is still very good (better than 10%) until  $r = 0.06$  Mpc is reached, the resolution limit of the MC<sup>2</sup> simulation. At the smallest radii  $r < 0.05$  Mpc HOT, HYDRA, and TPM are still in very good agreement while the GADGET profile is somewhat steeper. For comparison we plot a profile suggested by Navarro, Frenk, and White (1995) (“NFW profile” in the following) with the con-

centration parameter  $c = 7.12$ . We calculated the optimal concentration parameter based on the average mass and  $r_{200}$  obtained from our simulations using a publicly available code from Navarro<sup>2</sup>. The value we found is smaller than in the original SB paper where  $c = 7.5$  was chosen. The lower value here results from the higher cluster mass as compared to the original SB paper. The profile is an excellent match to the simulation results.

In Fig. 7 we show the result for the four  $256^3$  particle runs. Down to  $r = 0.06$  Mpc, the resolution limit for  $\text{MC}^2$ , FLASH, and GADGET in this simulation, the agreement of all runs is sub-8%, again excellent. (The agreement in the original paper was 20% or better.) In this simulation, only HOT was run with a very small smoothing length, thus at small radii it is the only code with enough resolution to provide converged results. The other three codes were run with roughly equivalent force resolution and they do provide consistent results at small radii, the fall-off of the halo density for  $r < 0.1$  Mpc resulting from the force smoothing. The corresponding NFW profile is shown for comparison.

In Figs. 8 and 9 the dark matter velocity dispersion profiles are shown for the  $128^3$  particle and  $256^3$  particle runs. In both cases the velocity dispersion peak is higher than in the original SB paper, 1250 km/s for the  $128^3$  runs and 1200 km/s for the  $256^3$  runs, while in the SB comparison the average maximum was around 1100 km/s. This could be due to the higher force resolutions in the present runs, a conclusion consistent with the higher  $\sigma_{DM}$  peak values obtained in the original paper by the higher-resolution codes. This argument can also be checked by the low-resolution FLASH- $128^3$  run: The maximum here is around 1000 km/s. The general agreement in both the  $128^3$  and  $256^3$  particle cases is very good for the outer shells, better than 5%. In the inner shells the agreement is better than 10%, with only the low-resolution FLASH- $128^3$  run disagreeing up to 20%. Following the results for the density profile, the overall agreement between the different runs is better by a factor of two than in the original SB paper. We do not observe a large scatter of the results in the last bin as reported in the SB paper. There it was argued that the scatter is due to noise arising from subclustering but we see no evidence to support this.

Finally, we compare the radial velocity profiles. The results are shown in Figs. 10 and 11. Net infall is seen at roughly the same radius as in the original paper, between 600 kpc and 700 kpc for both cases. The scatter in the  $128^3$  particle simulations is around 150 km/s (note that the residual here is quoted without the logarithm), while the scatter in the  $256^3$  simulations is slightly smaller with 100 km/s. The original SB result has a scatter of 200 km/s. Overall the agreement of the different codes is very satisfactory, however the  $256^3$  particle FLASH simulation shows a relatively high radial velocity in the inner region.

Our results for the Santa Barbara cluster comparison for the six tested codes are very positive. The agreement of all measured quantities across the codes is much better than in the original test. This could be due to several reasons: (i) Every code was run with exactly the same initial particle positions and velocities, resulting in a more uniform comparison (using only the initial density field can lead to slightly different initial conditions since every simulator would have to implement the Zel'dovich step to obtain positions and velocities). (ii) We used the same analysis code for all simulations, thereby eliminating

<sup>2</sup><http://pinot.phys.uvic.ca/jfn/mywebpage/home.html>

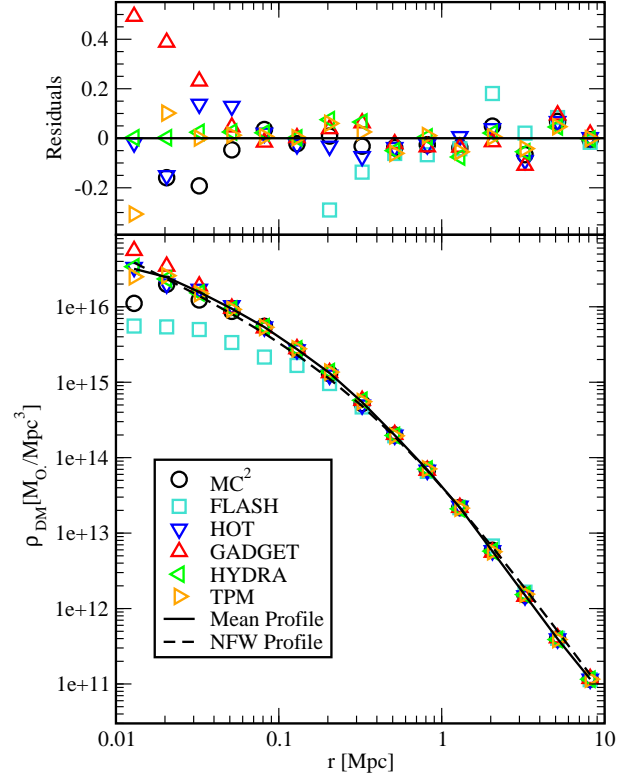


FIG. 6.— Dark matter density profile for the Santa Barbara cluster,  $128^3$  particles. The mean profile (solid curve) is a simple average over all the simulations, with the exception of the FLASH results.

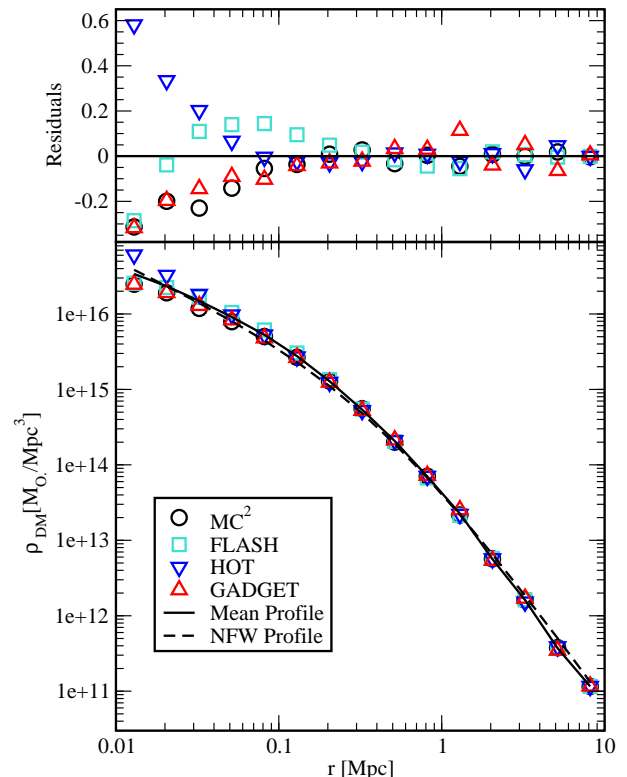


FIG. 7.— Dark matter density profile for the Santa Barbara cluster,  $256^3$  particle simulations.

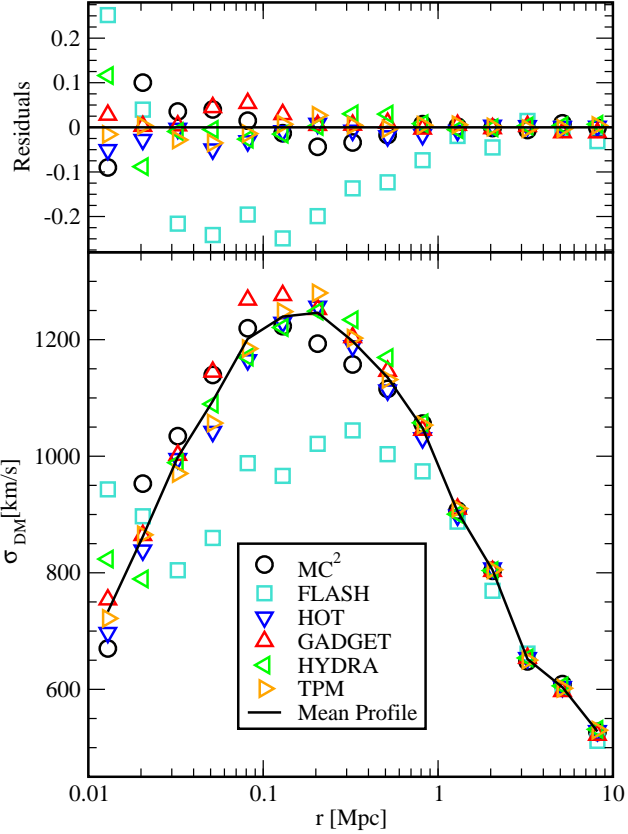


FIG. 8.— Dark matter velocity dispersion profile for the Santa Barbara cluster,  $128^3$  particles. The FLASH results are not included in the mean profile.

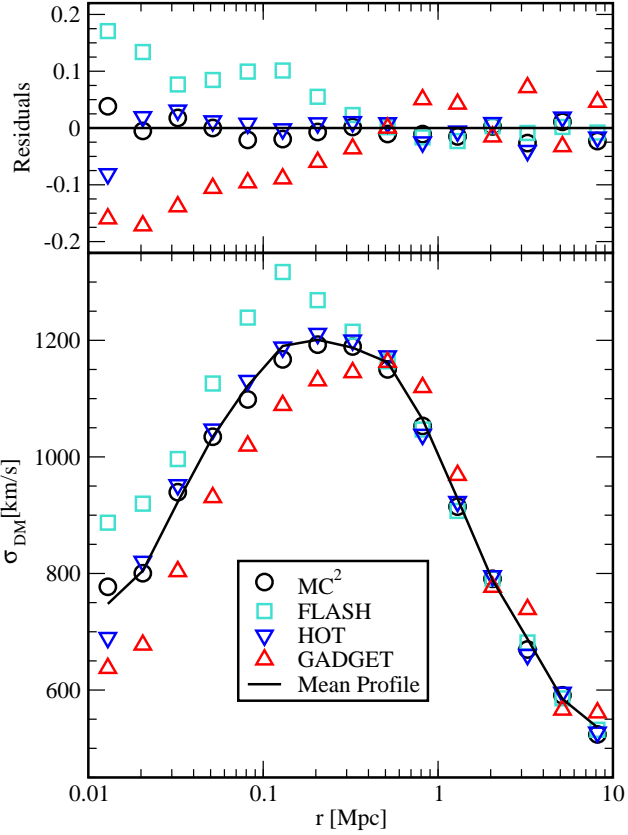


FIG. 9.— Dark matter velocity dispersion profile for the Santa Barbara cluster,  $256^3$  particle simulations.

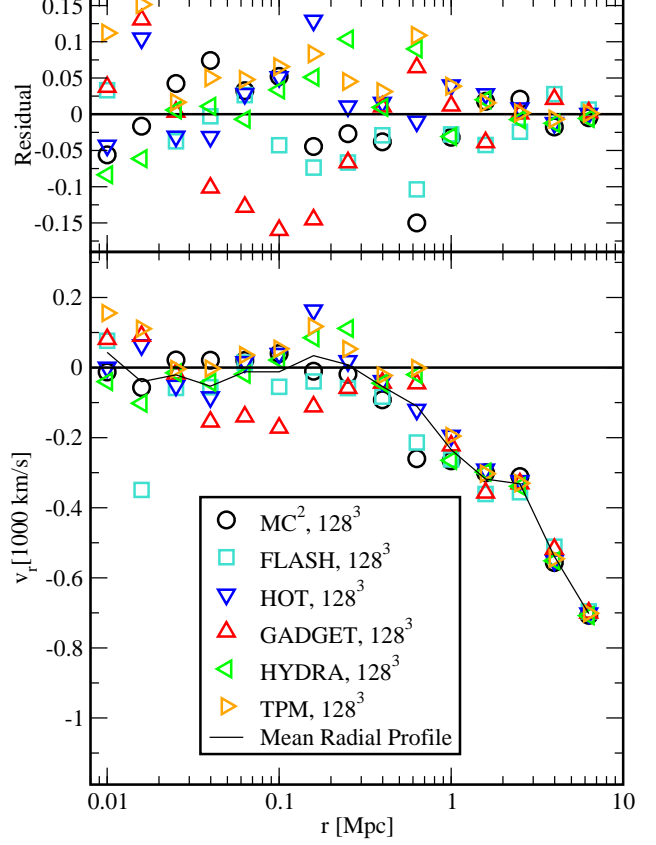


FIG. 10.— Dark matter radial velocity profile for the Santa Barbara cluster,  $128^3$  particles. The FLASH results are not included in the mean profile.

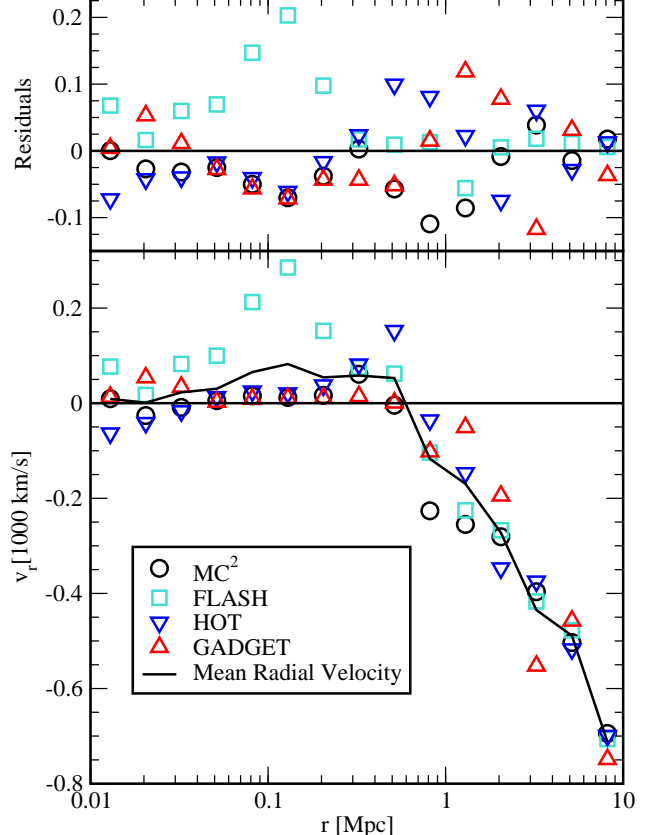


FIG. 11.— Dark matter radial velocity profile for the Santa Barbara cluster,  $256^3$  particle simulations.

any uncertainties introduced by variations in diagnostics routines, e.g., estimating the center of the cluster, etc. (iii) Most of the simulations were run with very similar resolution, varying from 5 kpc to 64 kpc for the high resolution runs, while the resolutions in the original test varied between 5 kpc and 960 kpc. (iv) The present test used dark-matter only simulations.

## 5. TESTS WITH THE COSMOLOGICAL CONCORDANCE MODEL

### 5.1. Test Description

In this Section, we study results from two realistic N-body cosmological simulations of a  $\Lambda$ CDM universe, a “small” 90 Mpc box and a “large” 360 Mpc box using  $256^3$  particles. These boxes straddle a representative range of force and mass resolutions for state-of-the-art large scale structure simulations designed to study power spectra, halo mass functions, weak lensing, etc. The 90 Mpc box is somewhat small as a representative simulation due to lack of large-scale power. Nevertheless, we chose this volume for code comparison because it allows a relatively high resolution for  $MC^2$ , which we are using as a collisionless standard.

The initial linear power spectrum was generated using the fitting formula provided by Klypin and Holtzman (1997) for the transfer function. This formula is a slight variation of the common BBKS fit (Bardeen et al. 1986). It includes effects from baryon suppression but no baryonic oscillations. We use the standard Zel’dovich approximation (Zel’dovich 1970) to provide the initial particle displacement off a uniform grid and to assign initial particle velocities. The starting redshift for both box-sizes is  $z_{in} = 50$ . In each case, we choose the following cosmology:  $\Omega_m = 0.314$  (where  $\Omega_m$  includes cold dark matter and baryons),  $\Omega_b = 0.044$ ,  $\Omega_\Lambda = 0.686$ ,  $H_0 = 71$  km/s/Mpc,  $\sigma_8 = 0.84$ , and  $n = 0.99$ . These values are in concordance with the measurements of cosmological parameters by WMAP (Spergel et al. 2003). Both simulations used  $256^3$  simulation particles, implying particle masses of  $1.918 \cdot 10^9 M_\odot$  for the small box and  $1.227 \cdot 10^{11} M_\odot$  for the large box.

The analysis of the runs is split into two parts. First, the particle positions and velocities and their two-point functions are studied directly. We measure velocity distributions, the mass power spectrum, and correlation functions, and compare position slices from the simulation box directly. Second, halo catalogs are generated and investigated. Here we compare velocity statistics, correlation functions, mass functions, and for some specific mass bins, the positions, masses, and velocities of selected individual halos.

The  $MC^2$ -simulations are carried out on a  $1024^3$  mesh for both physical box sizes. A detailed convergence study with  $MC^2$  will be presented elsewhere (Habib et al. 2004). For the test simulations, FLASH’s base grid is chosen to be a  $256^3$  mesh, with two levels of mesh refinement leading to an effective resolution equivalent to a  $1024^3$  mesh in high density regions. The softening length for the other four codes are chosen in such a way that sufficient resolution is guaranteed and reasonable performance on a Beowulf cluster is achieved. The softening lengths ranged between 10 to 40 kpc. In Table 3 the force resolutions from the different codes and runs are summarized. LCDMs refers to the 90 Mpc box simulation, LCDM<sub>b</sub> to the 360 Mpc box simulation.

### 5.2. Results

Following the conventions for the Santa Barbara test, we use the following color coding for the different codes in all compar-

ison plots:  $MC^2$  results are shown with black lines and circles, FLASH with turquoise lines and squares, HOT with blue lines and down-triangles, GADGET with red lines and up-triangles, HYDRA with green lines and left-triangles, and TPM with orange lines and right-triangles. As an arbitrary convention, all residuals shown are calculated with respect to the results from GADGET, rather than from an average over the results from all the codes. This is done mainly in order to avoid contaminations of averages from lower resolution results or from individual simulations with some other systematic source of error.

#### 5.2.1. Positions and Velocities of the particles

In order to first compare the codes qualitatively and picture the ‘cosmic web’ it is helpful to look at the particles directly. In Figs. 12 and 13 we show the results for the six codes. For the small box (Fig. 12) we cut out a 1 Mpc thick slice in the  $xy$ -plane through the center of the box. The velocities of the particles are divided into 4 equal bins between 0 and 440 km/s. Each particle is individually colored according to the bin it belongs to. The agreement of the 6 codes is very impressive, with a visual impression of almost particle by particle agreement (if one were to zoom in, this would of course not hold in the small-scale virialized regions). Even though the grid codes  $MC^2$  and FLASH were run at lower resolution than the other four codes, in this qualitative comparison they are almost indistinguishable from the higher resolution runs. The results for the big box are shown in Fig. 13. Here we have cut out a 3 Mpc thick slice in the  $xy$ -plane through the center of the box. Again, even though the resolutions of the different simulations are different, the plots are very similar.

#### 5.2.2. Velocity Statistics of the Particles

We now turn to a more detailed comparison of the particle velocities. We measure the distribution of the particle speeds  $v = \sqrt{v_x^2 + v_y^2 + v_z^2}$  in bins of 25 km/s for the small box and of 30 km/s for the large box. In order to compare the distributions from the different codes we only include velocities between 1 km/s and 2500 km/s in the small box and between 1 km/s and 3000 km/s for the big box. In the velocity distribution plots we have cut off the tail of the distributions to display more detail.

Let us first consider the results for the 90 Mpc box. In Fig. 14 the comparison of the velocity distribution for all 6 codes is shown. HOT, GADGET, HYDRA, and TPM are almost indistinguishable. In the upper panel of the plot the relative residual in comparison to GADGET is shown. The relative deviation of HOT, HYDRA and TPM from GADGET is below 3% up to 1500 km/s, while  $MC^2$  (on a  $1024^3$  mesh) and FLASH deviate in the main region of interest by less than 5%. By combining a  $512^3$  mesh simulation and the  $1024^3$  mesh simulation from  $MC^2$ , it is possible to predict the result for the continuum from the PM simulations by using Richardson extrapolation with linear convergence (the order of convergence was found numerically using a range of grid sizes). This reduces the systematic deviation from the higher resolution codes very significantly (less than 3% up to 1500 km/s), as evidenced by the top panel of Fig. 14. The main significance of this result lies in the fact that  $MC^2$  is not collisional up to the resolution employed in the cosmological tests, thus the Richardson extrapolation to a higher effective resolution does not bring in any artificial heating from collisions. The much improved agreement with the higher resolution codes is strong evidence that, over the velocity range studied, collisional effects are subdominant in those

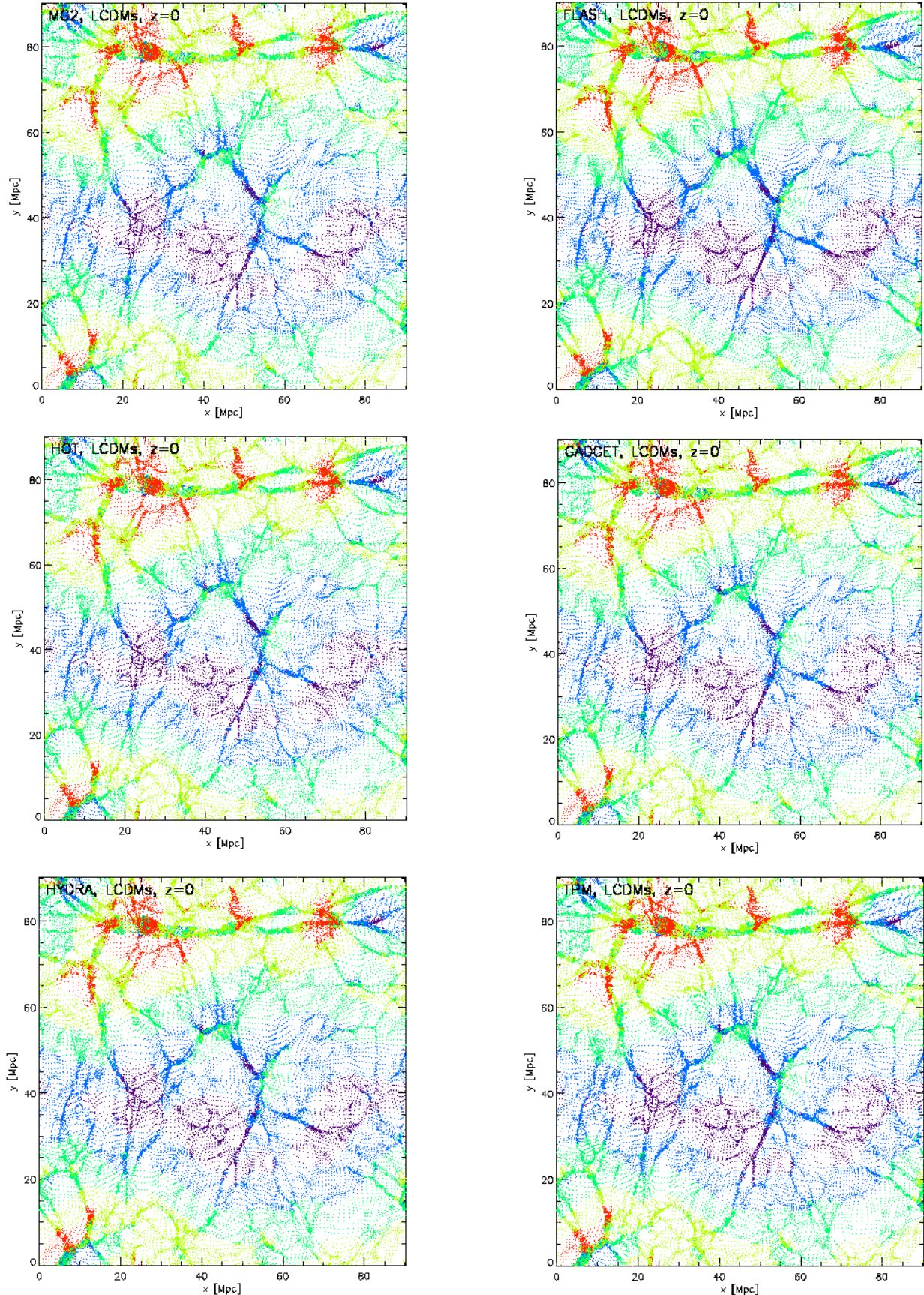


FIG. 12.— Comparison of the particle positions and velocities in a 1 Mpc thick slice of the 90 Mpc box. The colors show four (uniform) velocity bins between 0 and 440 km/s. Dark blue corresponds to a velocity between 0 and 110 km/s, light blue to a velocity between 110 km/s and 220 km/s, dark green to a velocity between 220 km/s and 330 km/s, and red corresponds to the highest velocities between 330 km/s and 440 km/s.

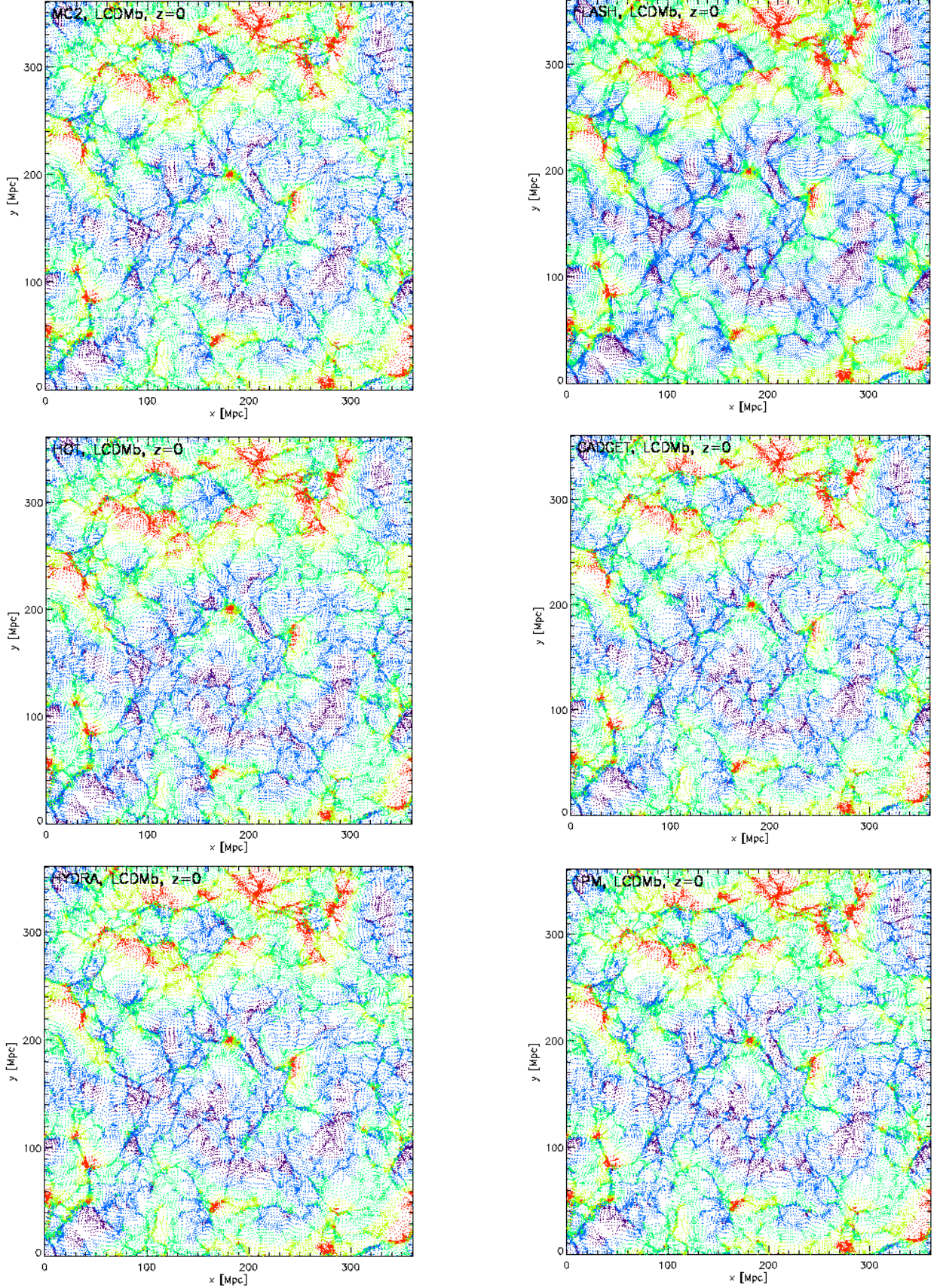


FIG. 13.— Comparison of the particle positions and velocities in a 3 Mpc thick slice of the 360 Mpc box. As in the small box, the velocities are divided into 4 equal bins of size 175 km/s with a similar color-coding, the maximum speed being 700 km/s.

TABLE 3  
SOFTENING LENGTHS/MESH SPACINGS FOR THE  $\Lambda$ CDM RUNS

	MC <sup>2</sup>	FLASH	HOT	GADGET	HYDRA	TPM
LCDMs, $256^3$ particles	90 kpc	90 kpc	10 kpc (physical after $z=9$ )	20 kpc	40 kpc	10 kpc
LCDMb, $256^3$ particles	350 kpc	350 kpc	20 kpc (physical after $z=9$ )	20 kpc	40 kpc	20 kpc

codes as well. [Details of the extrapolation methodology and how it may be used to improve resolution for mesh codes will be provided in a forthcoming paper (Habib et al. 2004).] The deviation of FLASH from GADGET is very similar to the deviation of the  $1024^3$  simulation from MC<sup>2</sup>, indicating that most relevant regions were refined in the FLASH simulation to the highest level. Overall, this first quantitative comparison may be considered very satisfactory.

Next, we analyze the corresponding results for the 360 Mpc box. The comparison of all six codes is shown in Fig. 15. Overall, the results are not as good as for the smaller box. Nevertheless, HYDRA and TPM agree with GADGET at better than 8% over the whole range and better than 2% up to 1500 km/s. The velocities generated by HOT are overall slightly higher, however, the agreement with the other codes is still around 6% over most of the range. The raw MC<sup>2</sup> and FLASH results deviate from the higher resolution runs up to 40% for very large velocities as the grid resolution is not adequate to resolve high density regions properly. Once again, Richardson extrapolation using a  $512^3$  and a  $1024^3$  mesh succeeds in converting the MC<sup>2</sup> results to those indistinguishable from the higher-resolution simulations (less than 3% difference from GADGET in the region

of interest). Note that at large velocities, systematic deviations across the codes, though small, are clearly visible, especially in the large box.

Around the peak of the distribution, MC<sup>2</sup> performs slightly better than FLASH. This is easy to understand: As velocities are highest in the high density regions (e.g., the clumped regions in Fig. 13), the effective resolution in these regions controls the accuracy with which the tail of the velocity distribution is determined. Fig. 16 shows a log-density slice from the simulation with the AMR-grid superimposed onto it. The high density regions are appropriately refined by FLASH (smaller submeshes). However, the lower density regions are treated with poorer resolution, therefore, we expect good agreement with a  $1024^3$  mesh simulation for the higher velocities, and for the lower velocities, good agreement with the corresponding resolution PM simulation. In Fig. 17 we show the relative residuals with respect to GADGET of the  $512^3$  mesh and  $1024^3$  mesh MC<sup>2</sup> simulations, and the AMR-FLASH simulation. In the high velocity tail the higher resolution simulation from MC<sup>2</sup> and FLASH agree very well, while for the lower velocity region the MC<sup>2</sup>  $512^3$  mesh simulation agrees better with FLASH (at late times, near  $z=0$ , the main box is run by FLASH at a

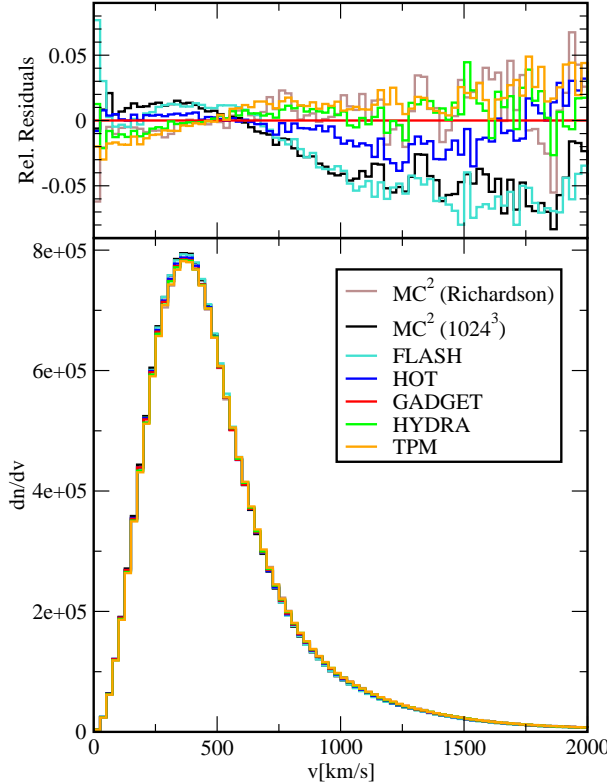


FIG. 14.—Particle velocity distribution for all six codes at  $z=0$ , 90 Mpc box. The upper panel shows the relative residuals in comparison with GADGET.

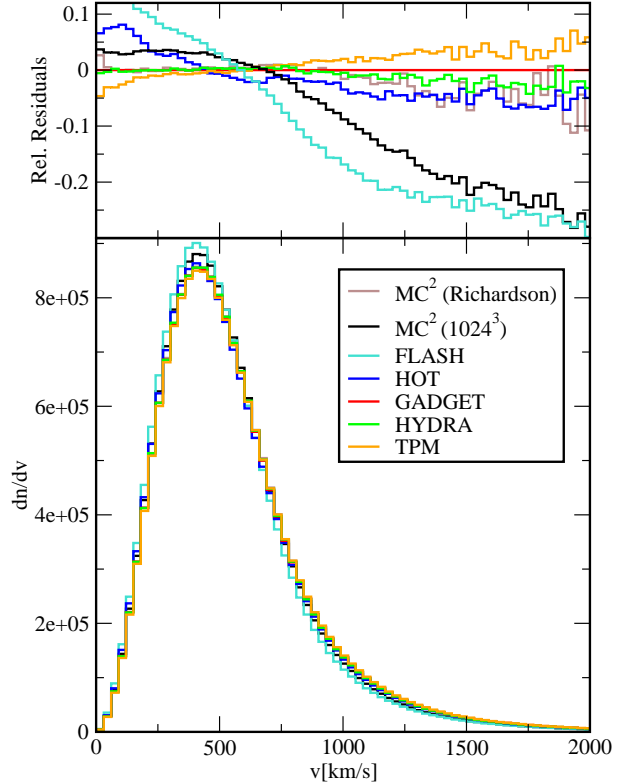


FIG. 15.—Particle velocity distribution following Fig. 14 for the 360 Mpc box. Note the small systematic deviations at high velocities.

resolution of  $512^3$ ).

Finally, we compare results for  $v_{12}(r)$ , the (pair-averaged) relative pairwise streaming velocity considered as a function of the separation  $r$  between two mass tracers. If the tracers are dark matter particles then the pair conservation equation [following the standard BBGKY approach (Davis and Peebles 1977, Peebles 1980)], connects the  $v_{12}(r)$  field to the two-point correlation function of the particle distribution  $\xi(r)$ . Measurements of  $v_{12}(r)$  from peculiar velocity surveys provide useful constraints on  $\Omega_m$  and  $\sigma_8$  (Feldman et al. 2003). While theoretical predictions for these measurements are best carried out with the corresponding velocity statistics for halos, computing  $v_{12}(r)$  for particles and comparing this with the same quantity calculated for halos is used to determine halo velocity bias. The pairwise peculiar velocity dispersion  $\sigma_{12}(r) = \langle [\mathbf{v}(\mathbf{r}) - \langle \mathbf{v}(\mathbf{r}) \rangle]^2 / 3 \rangle^{1/2}$  is also an important statistical quantity, connected to  $\Omega_m$  and the two-point correlation function via the Cosmic Virial Theorem (Peebles 1976a and 1976b).

Results for the two quantities are displayed in Figs. 18 and 19 for the small and large boxes respectively. Absolute residuals with respect to GADGET are provided for the  $v_{12}(r)$  results (since  $v_{12}$  can vanish), while relative residuals are given for  $\sigma_{12}(r)$ . The  $v_{12}$  results for the small box show a small bump in the GADGET results with respect to the other codes at  $r \simeq 0.5$  Mpc, otherwise the results are better than 10%, and, in the actual range of physical interest,  $r > 1$  Mpc, (except for the FLASH results), the agreement is better than 5%. The results for  $\sigma_{12}(r)$  from the high resolution codes are very good, with agreement at the few % level achieved, except on small scales where resolution limitations are manifest. The results from the lower-resolution mesh codes, as expected, show a small 5% suppression in  $\sigma_{12}(r)$  in the region of the peak. (Here we have not attempted extrapolation to improve the results.) Results from the large box for  $v_{12}$  again show a systematic difference between the other high-resolution codes and GADGET

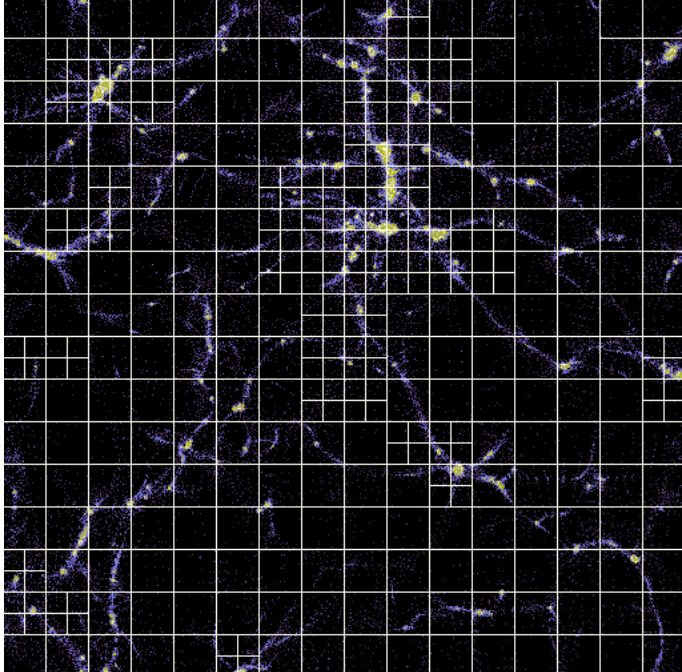


FIG. 16.— Refined mesh from a FLASH-AMR simulation superposed on a partial density slice from the center of the 360 Mpc simulation box.

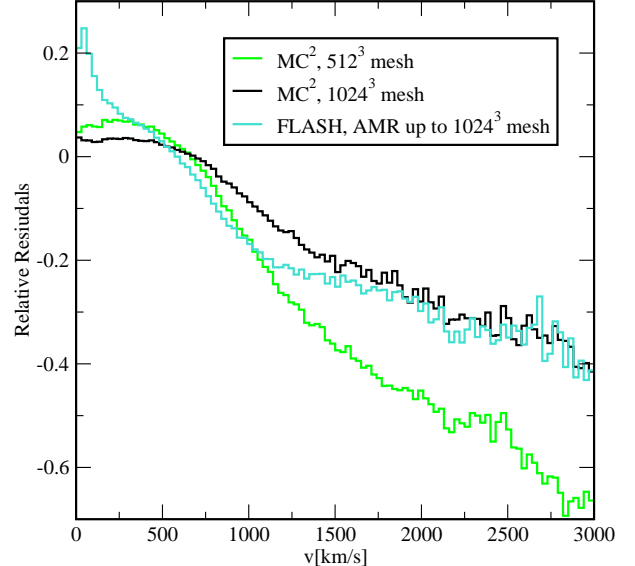


FIG. 17.— Comparison of the relative residuals for particle velocities from the  $MC^2$   $512^3$  grid and  $1024^3$  grid runs with the FLASH results, 360 Mpc box. See the text for a discussion.

at roughly 10% in the region around 1 Mpc. The results for  $\sigma_{12}(r)$  for the high-resolution codes are very consistent, with better than 5% agreement across the range. The mesh codes (without extrapolation) are at a particular disadvantage in this test since the peak in  $\sigma_{12}(r)$  occurs relatively close to their resolution limit.

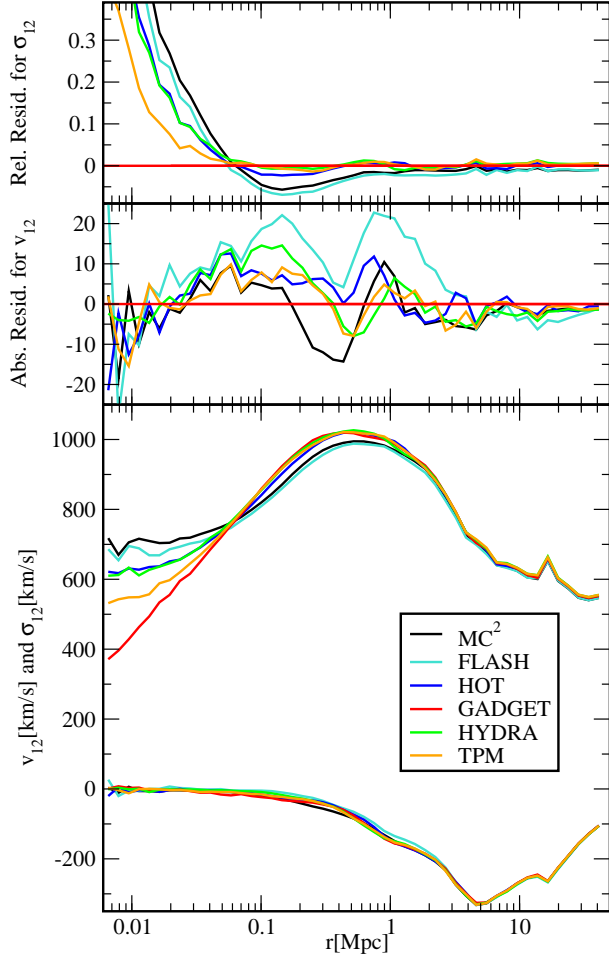


FIG. 18.— Comparison of the relative particle pairwise streaming velocity  $v_{12}(r)$  (lower set of curves) and the pairwise peculiar velocity dispersion  $\sigma_{12}(r)$  (upper set) for all six codes at  $z = 0$ , 90 Mpc box.

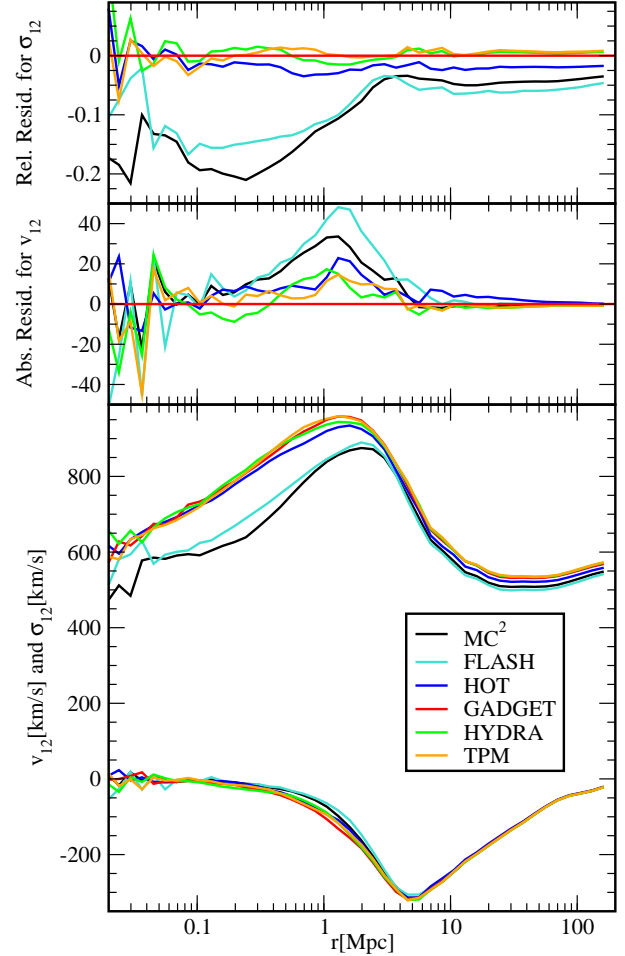


FIG. 19.— Comparison of the relative particle pairwise streaming velocity  $v_{12}(r)$  (lower set of curves) and the pairwise peculiar velocity dispersion  $\sigma_{12}(r)$  (upper set) for all six codes at  $z = 0$ , 360 Mpc box.

### 5.2.3. Power Spectrum of the Particle Density Field

The next quantitative comparison performed for the particles is the measurement of the power spectrum  $P(k)$ . The power spectrum is obtained in the following way: First the density is calculated with a CIC (Cloud-In-Cell) scheme on a  $1024^3$  spatial grid. Then a  $1024^3$  FFT is employed to obtain the density in  $k$ -space and squared to yield the power spectrum. (In order to compensate for the CIC softening we deconvolve the  $k$ -space density with the CIC window function.) Finally, the three-dimensional power spectrum is binned to get the one-dimensional power spectrum. We did not attempt to compensate for particle shot noise or use a bigger FFT as the aim here is to look for systematic differences between codes rather than actually obtain a more accurate  $P(k)$ . The power spectrum will be studied in more detail in later work.

We begin again with the small box, the results being shown in Fig. 20. The lower panel shows the results from the six codes and in addition a power spectrum generated by Richardson extrapolation from a  $512^3$  and a  $1024^3$  mesh  $MC^2$  simulation. The upper panel displays the relative residuals with respect to GADGET. The agreement between the HOT, GADGET, HYDRA, and TPM is very good, better than 10% up to  $k = 10 \text{ Mpc}^{-1}$ . For higher  $k$  the HOT and HYDRA simulations have slightly less power than the GADGET and TPM simulations. The results from the two mesh codes,  $MC^2$  and FLASH, are in good agreement with the other runs up to a few  $\text{Mpc}^{-1}$ . For higher  $k$ , the limited resolution of these two runs leads to larger discrepancies, as expected. In these runs, the slightly higher resolution of  $MC^2$  compared to FLASH is again visible. The Richardson extrapolation result from  $MC^2$  differs from the GADGET simulation by roughly 5% up to  $k=10 \text{ Mpc}^{-1}$ . For larger  $k$  the difference becomes much larger. This is as expected since the extrapolation procedure cannot generate power which was not present in the underlying simulations; it can only improve the accuracy of the results on scales where convergence holds. Due to this property, it functions as an excellent test of code convergence.

Next we compare the results for the large box, as shown in Fig. 21. The overall result is very similar to the small box. Over roughly two orders of magnitude in  $k$  the high resolution runs from HOT, GADGET, HYDRA, and TPM agree better than 5%. The TPM simulation agrees with GADGET over the entire range to better than 2%. The HYDRA run shows again a slight fall-off of the power with  $k$  before the other high resolution codes do. The results from HOT appear to be systematically low in the normalization. The  $MC^2$  result shows good agreement (sub-5%) with GADGET up to  $k=1 \text{ Mpc}^{-1}$ , while the FLASH power spectrum falls off faster already at  $k=0.4 \text{ Mpc}^{-1}$ . This is consistent with the fact that in the large box less of the volume was refined (14.3%) than in the small box (40.8%). As seen for the small box, Richardson extrapolation again leads to a large improvement: the difference with GADGET becomes sub-5% up to  $k=4 \text{ Mpc}^{-1}$ .

As with the results obtained for the particle velocity statistics, the results for the power spectrum are also very satisfactory. From the point of view of force resolution, all six codes agree over the  $k$ -range for which consistent results are to be expected: The four high resolution codes agree at the sub-5% level in the main regions of interest, while the the results for the two mesh codes are also consistent with the expected resolution and convergence properties of these codes.

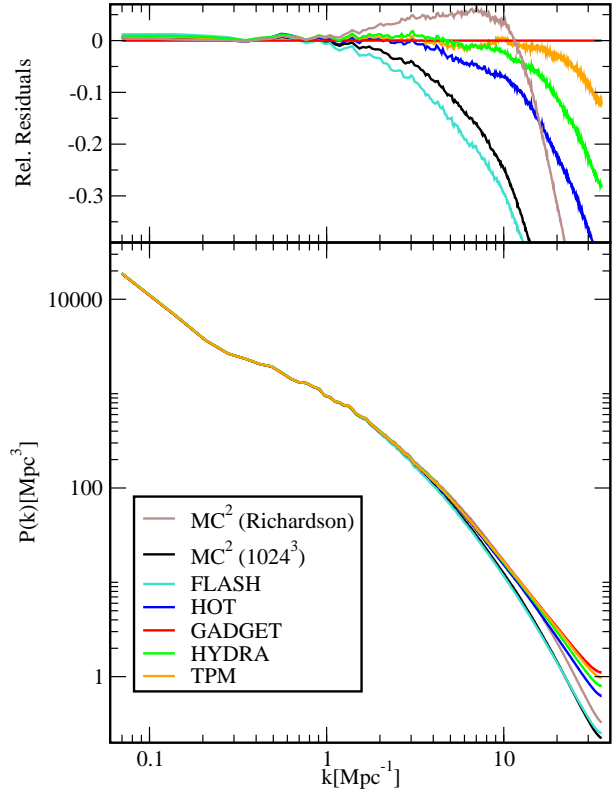


FIG. 20.— Comparison of the density power spectra for all six codes at  $z = 0$ , 90 Mpc box. The Richardson-extrapolated result from  $MC^2$  is also shown.

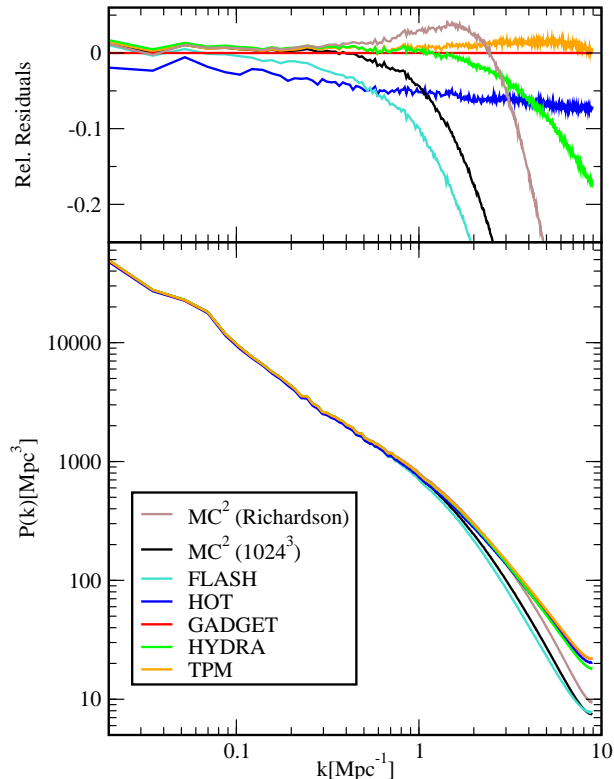


FIG. 21.— The density power spectrum results for the 360 Mpc box, following Fig. 20.

#### 5.2.4. Particle Correlation Function

After comparing the power spectrum we now investigate its real-space counterpart, the correlation function generated from the particle positions. The  $O(N^2)$  calculation is straightforward, though tedious. In principle the correlation function contains the same information as the power spectrum, however, since they were obtained in different ways, comparison against the correlation function provides a simple cross-check. The correlation functions were generated by randomly choosing 65,536 particles from each simulation, and calculating the number of particles contained within logarithmically spaced radial bins using a direct  $N^2$  search.

The results for the small box are shown in Fig. 22. As always, the lower panel shows the results from the six different codes while the upper panel displays the relative residuals with respect to the GADGET simulation. The agreement of all codes is very good for large  $r$ , between 200 kpc and 40 Mpc, the deviation from GADGET for all other codes being less than 5%. For  $r$  smaller than 200 kpc the limited resolution of the  $MC^2$  and FLASH simulations becomes apparent, the correlation function falling off much faster than for the other simulations. At  $r \approx 20$  kpc the correlation function from GADGET rises much more steeply than from the other simulations. At this point the resolution limit of GADGET (see Table 3) is being reached so these results should not be interpreted as a code problem. In fact, this rise may be due to the adaptive timestep integrator in GADGET using more timesteps for the particles in high-density regions than the other codes. For this reason, the large relative residuals with respect to GADGET should not be taken seriously at small scales. Up to this point HOT, HYDRA, and TPM agree better than 5% with GADGET.

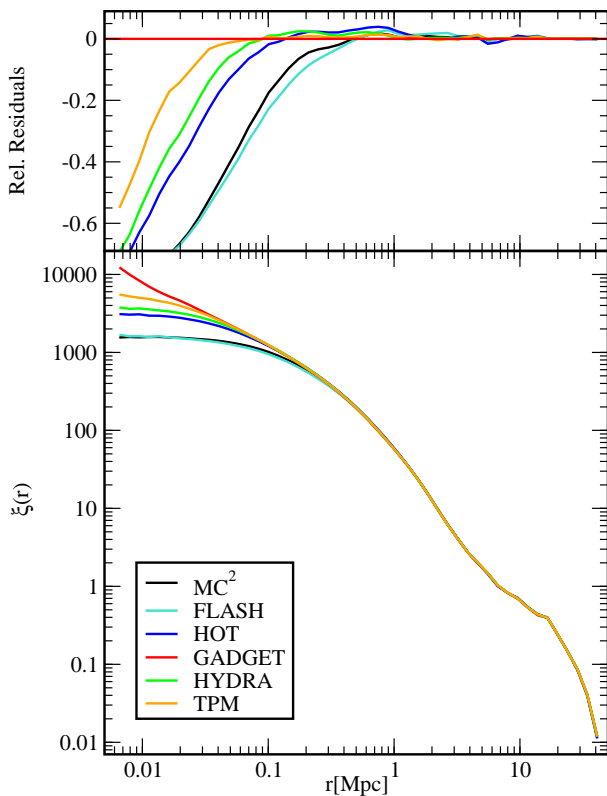


FIG. 22.—Comparison of the particle two-point correlation functions from the six codes at  $z = 0$  for the 90 Mpc box.

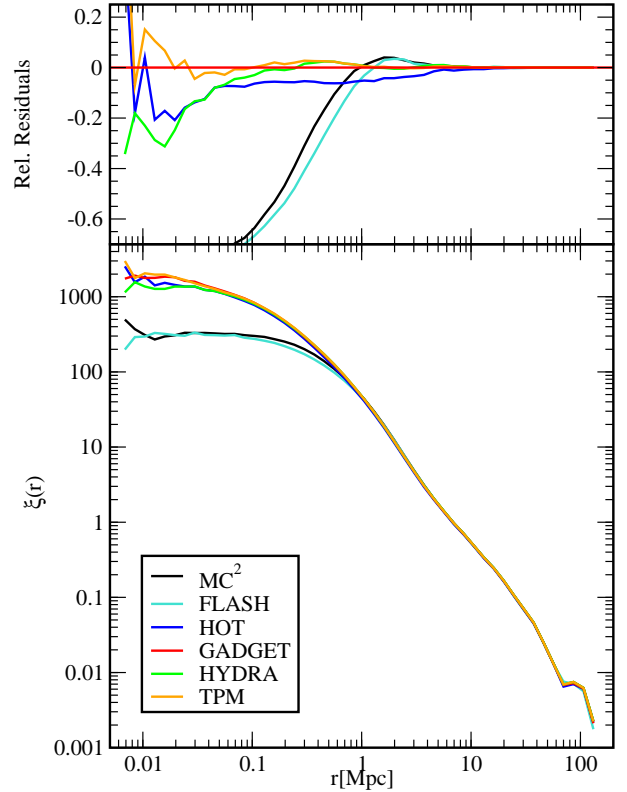


FIG. 23.—The particle two-point correlation function for the 360 Mpc box, following Fig. 22.

The results for the large box are shown in Fig. 23 and are similar to those from the small box. For large  $r$  the agreement is once again excellent, between 0.8 Mpc and 160 Mpc all codes agree to better than 5%. At small  $r$ , FLASH and  $MC^2$  suffer from degraded resolution, and the disagreement between the other codes becomes larger. The correlation function from HOT is systematically lower in the region  $0.1 \text{ Mpc} < r < 5 \text{ Mpc}$ , while HYDRA's correlation function, due to the slightly lower resolution employed than HOT, GADGET, and TPM, falls off a little earlier than GADGET and TPM. For very small  $r$  the discrepancy between the codes is at the 10% level, but here the codes are being pushed too close to their resolution limits.

Overall, as expected, the results for the correlation functions are very similar to those for the power spectrum. The resolution limits of the grid codes  $MC^2$  and FLASH are clearly exposed at the correct scales, with the four high resolution codes agreeing well with each other until scales close to the resolution limits are reached.

#### 5.2.5. Halo Mass Function

We now turn from comparing particle position and velocity statistics to comparing results extracted from halo catalogs. In many ways, it is the halo information that is of more direct relevance to comparison with cosmological observations, so these tests are of considerable importance. The halo catalogs were generated using a Friends-Of-Friends (FOF) algorithm (Davis et al. 1985). This algorithm defines groups by linking together all pairs of particles with separation less than  $b\bar{n}^{-1/3}$ , where  $\bar{n}$  is the mean particle density. This leads to groups bounded approximately by a surface of constant local density,  $\rho/\bar{\rho} \approx 3/(2\pi b^3)$ . We have chosen a linking length of  $b = 0.2$  corresponding to a density threshold  $\rho/\bar{\rho} \approx 60$ . As discussed in Lacey & Cole

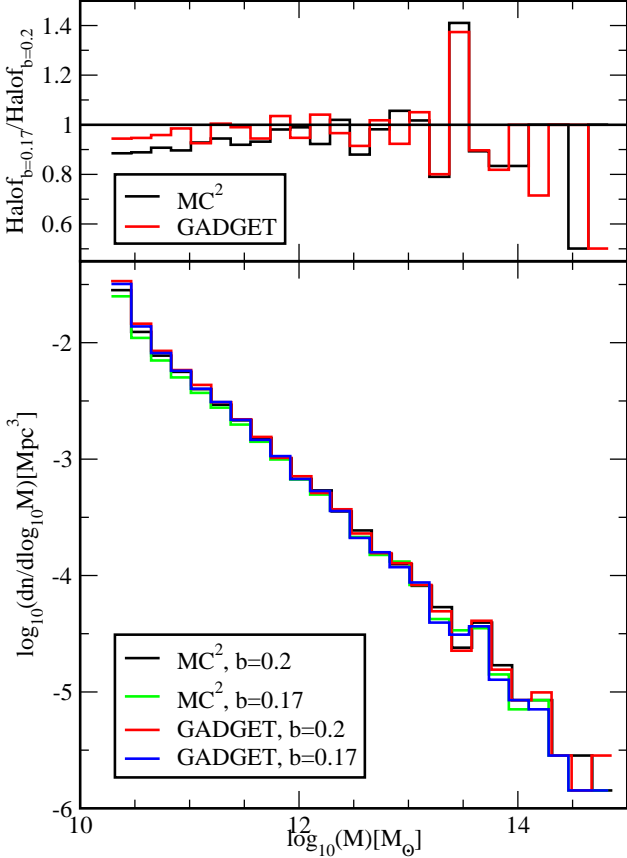


FIG. 24.— Comparison of results from two FOF halo finders with linking lengths of  $b = 0.2$  and  $b = 0.17$  run on the  $MC^2$  and GADGET simulations at  $z = 0$  for the 90 Mpc box. The top panel shows the ratio of the  $b = 0.17$  mass function and the  $b = 0.2$  mass function for the two codes.

1994, for a spherical halo with a density profile  $\rho(r) \propto r^{-2}$ , this local density threshold corresponds to a mean overdensity  $\langle \rho \rangle / \bar{\rho} \approx 180$ .

In order to confirm the results obtained with this halo finder we also analyzed two of the small box simulations (GADGET and  $MC^2$ ) with a different FOF halo finder<sup>3</sup> with a linking length of  $b = 0.17$  corresponding to a density threshold  $\rho / \bar{\rho} \approx 97$ . (For a discussion on the dependence of the mass function on the chosen linking length for a FOF halo finder, see, e.g., Lacey & Cole 1994.) We checked that the two FOF halo finders gave the same results for  $b = 0.17$ .

The comparison between the halo mass functions for the two choices of linking length is shown in Fig. 24. In the lower panel the mass functions found with the two halo finders for GADGET and  $MC^2$  are shown. In the upper panel we show the ratio of the two mass function results for  $MC^2$  and the ratio of the two mass functions found for GADGET. The ratio is the  $b = 0.17$  mass function divided by the  $b = 0.2$  mass function. The smaller linking length should find fewer halos in the small mass region and tend to “break up” heavier halos in the high mass region. Consequently the ratio should show a dip at both extremes (since there are far fewer high mass halos, overall the smaller linking length will lead to fewer halos). Our results are very consistent with this expectation and also with the fact that more  $MC^2$  halos are “lost” by the  $b = 0.17$  finder at small masses – due to the lower resolution, these halos are

<sup>3</sup>We thank Stefan Gottlöber for generating the alternate set of halo catalogs.

more diffuse as compared to the GADGET halos.

Discounting the high mass end, there is still a systematic variation of up to 10% in the two halo mass functions. This result should be kept in mind when comparing the mass function to semi-analytic fits: even the same type of halo finder with slightly different parameter choices can easily affect the mass function at the several % level. Furthermore, changing the mass resolution can also lead to systematic effects on halo masses using the same FOF algorithm. These aspects will be considered in detail elsewhere (Warren et al. 2005).

Next we analyze the halo catalogs generated with the same FOF halo finder for all six codes. We start by comparing the numbers of halos found in the different simulations. The results are listed in Table 4. The smallest halos considered contain 10 particles, leading to a minimum halo mass for the small box of  $2 \cdot 10^{10} M_\odot$ . In this box, the most massive halos have masses of the order of  $7 \cdot 10^{14} M_\odot$ . Allowing 10 particles to constitute a halo is a somewhat aggressive definition, and we are not arguing that this is appropriate for cosmological analysis. However, as a way of comparing codes, the very small halos are the ones most sensitive to force resolution issues and therefore tracking them provides a useful diagnostic of resolution-related deficiencies as well as providing clues to other possible problems.

Largely due to the generous definition of what constitutes a halo, the variation in the total number of halos is rather large: For the small box, HOT, GADGET and HYDRA found the largest number of halos, around 55000, while FLASH and TPM found almost 40% fewer halos. The number of halos from the  $MC^2$  simulation is in between these two extrema, a little closer

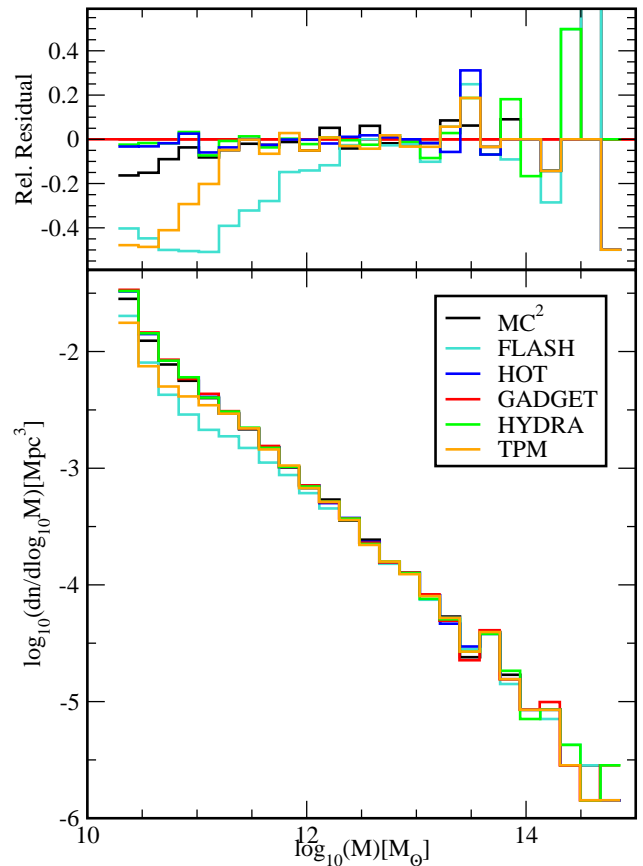


FIG. 25.— Comparison of the halo mass function for all six codes at  $z = 0$ , 90 Mpc box. See the text for a discussion of code systematics.

TABLE 4  
NUMBERS OF HALOS FOUND IN THE DIFFERENT SIMULATIONS

	MC <sup>2</sup>	FLASH	HOT	GADGET	TPM	HYDRA
LCDMs	49087 halos	32494 halos	54417 halos	55854 halos	34367 halos	54840 halos
LCDMb	65795 halos	33969 halos	73357 halos	72980 halos	55967 halos	74264 halos

to the higher numbers. For the large box the agreement of the number of identified halos from HOT, GADGET, and HYDRA, around 73000, is much better, but again the TPM simulation leads to almost 20000 fewer halos, and from the FLASH simulation, only 33000 halos were identified. The result from MC<sup>2</sup> is slightly lower than the results from HOT, GADGET, and HYDRA but much higher than the halos identified from TPM and FLASH.

We have generated mass functions from the different halo catalogs using a FOF algorithm with linking length  $b = 0.2$ . The comparison of the mass functions is shown in Fig. 25. As mentioned above, far fewer halos were found in the FLASH and TPM simulations, which becomes very apparent in this figure: At the low mass end of the mass function the results from these two codes are discrepant up to 40%. In contrast, MC<sup>2</sup>, HOT, GADGET, and HYDRA agree very well, to better than 5%.

In case of the grid codes, the fall-off at the low-end of the mass function can be easily connected to the resolution limit. To see this, given a particular halo mass, one computes a corresponding scale radius, say, e.g.,  $r_{180}$  and compares this with the grid resolution,  $\Delta$ . The scale radius  $r_{180}$  is defined to be such that the mean matter density within it is 180 times the mean background density (numerically, its value is roughly that of the virial radius). Clearly, if  $\Delta > r_{180}$ , halos in the particular mass region will be suppressed, as the finite force resolution will prevent the formation of compact objects on this scale. We have verified that the threshold for the fall-off in the mass function for MC<sup>2</sup> is set by the approximate condition  $\Delta \sim r_{180}$  in both the small and large boxes. One may wonder whether the lack of smaller halos has any effect on the mass function at masses higher than the resolution threshold set by  $\Delta \sim r_{180}$ . As shown by our results from both the mass function, and the comparison of individual halo masses below, this is not the case. The particles that would have ended up in smaller halos are not lost, and end up streaming into the larger halos so that there is no systematic bias in the mass function above the resolution threshold.

The result found for FLASH is also easy to understand. The base grid in the FLASH simulation was chosen to be  $256^3$  which was then refined up to  $1024^3$ , as explained above. At the beginning of the simulation this base resolution is not sufficient to form small halos. As the simulation proceeds forward in time, the resolution increases only where the density crosses the AMR threshold, elsewhere the small halos cannot be recovered. Therefore AMR codes will lead to very good results for the large halos and their properties, since for these the mesh will be appropriately refined. But without the implementation of AMR-specific initial conditions which help to solve the problem of starting with a pre-refined base grid, the mass function will be suppressed for small masses. This work is now in progress (Lukic et al. 2005). The condition  $\Delta \simeq r_{180}$  imposed using the base  $256^3$  grid correctly predicts the fall-off point in the mass function for the FLASH simulations. [A similar result for the mass function was found by O’Shea et al. (2003), in

which GADGET was compared to ENZO, an AMR-code developed by Bryan & Norman (1997,1999): The mass function from the ENZO simulation was lower for small masses than the one obtained from GADGET.]

We are unable to explain the fall-off in the mass function for the TPM simulations (seen in both the small and large boxes) in terms of a simple force resolution argument. It is possible that this effect is due to the grid-tree hand-off, but at present this remains a speculation.

The results for the large box show trends similar to the small box results. The overall agreement of the six codes shown in Fig. 26 is better than for the small box. The mass function from the TPM simulation is again lower than the others by roughly 40% for the small mass halos. The FLASH result for the small halos is up to 60% lower than that from GADGET. As in the small box, the condition  $\Delta \simeq r_{180}$  determines the mass below which halos are lost. The deviation from GADGET for the other codes is less than 2% over a large range of the mass function, a pleasing result.

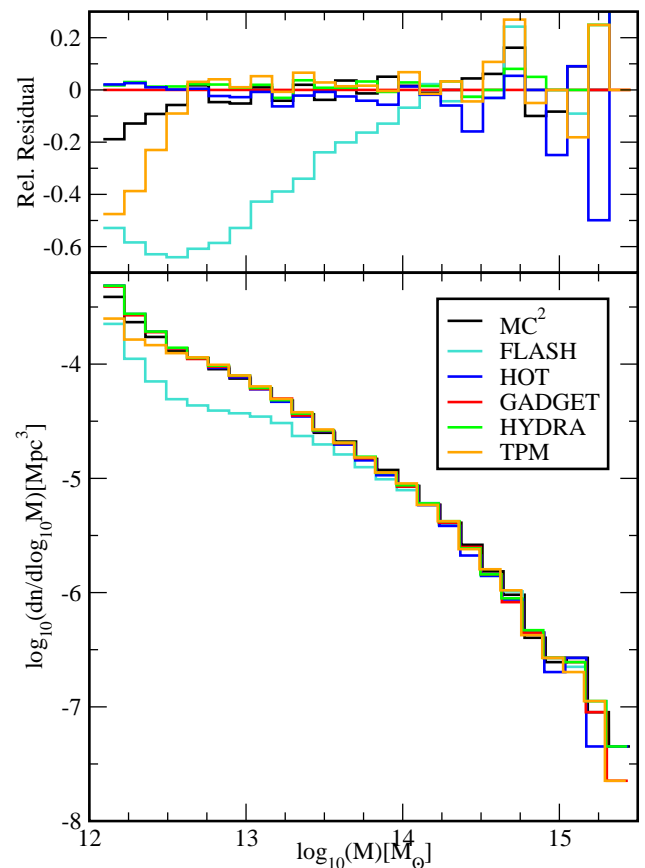


FIG. 26.— Comparison of the halo mass function for all six codes at  $z = 0$ , 360 Mpc box. For discussion of code systematics, see text.

### 5.3. Halo Power Spectrum

The distribution of dark matter halos is biased with respect to the overall distribution of the dark matter (Mo and White 1996). One way of estimating this bias is to compare the halo power spectrum with the (linear or nonlinear) power spectrum of the particle density field. Another method is to compare the respective correlation functions (halo-halo vs. particle-particle) (Colin et al. 1999, Kravtsov and Klypin 1999). We discuss both the halo power spectrum and the correlation function below.

In order to minimize problems with selection effects due to the differing code force resolutions and possible systematic uncertainties with halo finders, for the spatial analysis of halos we selected only those halos with more than a 100 particles. In the small box, this implies a halo mass threshold of  $2 \cdot 10^{11} M_{\odot}$  which, as comparison with Fig. 25 shows, succeeds in avoiding the low halo mass region where  $MC^2$  and TPM are somewhat deficient. For the larger box, the corresponding halo mass threshold is  $1.2 \cdot 10^{13} M_{\odot}$  which also avoids the low-mass region (Fig. 26). For both boxes the FLASH results, because of the AMR issues discussed above, continue to have fewer halos until a higher threshold is reached. In the small box there are roughly 6000 halos for each code, except for FLASH which had less than 5000.

The halo power spectrum was computed in essentially the same way as the particle power spectrum in Sec. 5.2.3 by first generating a CIC density field and then using a  $512^3$  FFT. Since the number of halos is much smaller than the number of particles, here shot noise subtraction is essential to obtain physically sensible results at small scales. We show both the noise-

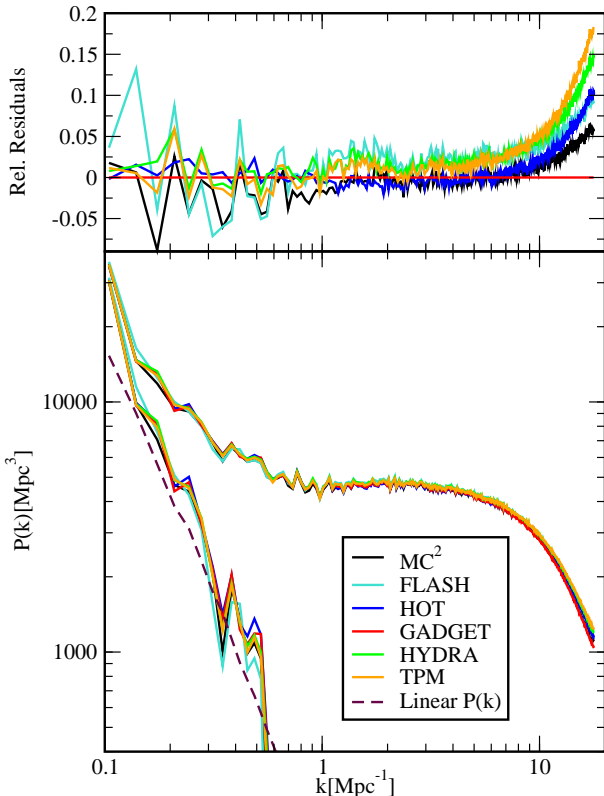


FIG. 27.— Comparison of the halo power spectrum for all six codes at  $z = 0$ , 90 Mpc box. The upper set of curves in the lower panel have not been noise-subtracted. The dashed line is the linear power spectrum from the corresponding initial condition realization.

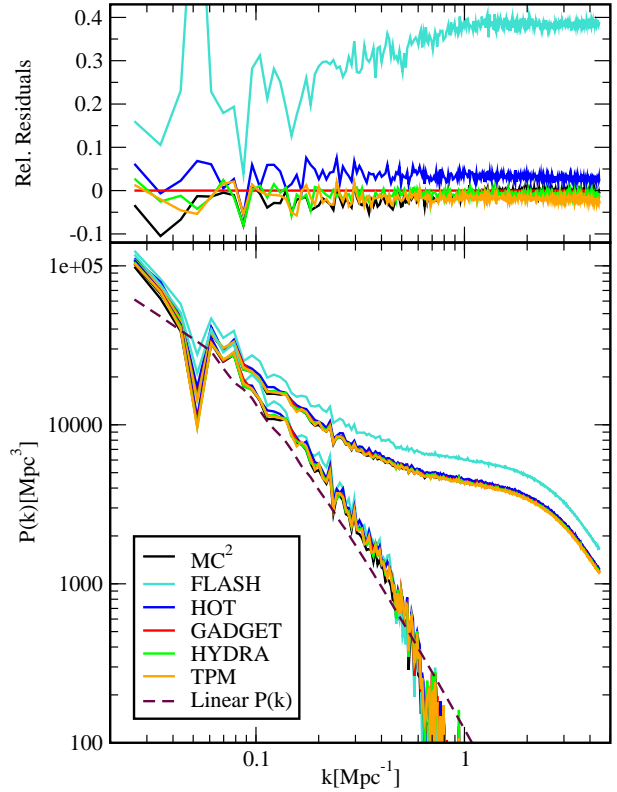


FIG. 28.— Comparison of the halo power spectrum for all six codes at  $z = 0$ , 360 Mpc box, following Fig. 27

subtracted and raw halo power spectra in Figs. 27 and 28 for the small and large boxes respectively. However, for code comparison purposes the direct halo power spectra are more relevant as noise subtraction induces large changes in the power spectra. Therefore, the relative residuals are computed for these quantities.

The results for the small box show a roughly 5% deviation till  $k = 10 \text{ Mpc}^{-1}$ . Note that this agreement is much better than the case for the particle power spectrum where the large  $k$  regime is dominated by small-scale particle motions. The case for the large box is very similar except for the FLASH results. The reason why the FLASH results are higher is because, (i) as earlier noted, there are fewer halos overall and (ii) the small mass halos are disproportionately absent with a resulting increase in bias.

#### 5.3.1. Halo Correlation Function

The halo correlation functions were computed in the same way as the particle correlation function in Section 5.2.4. Unlike the statistics of the raw particle distribution, these correlation functions provide a more direct measure of the galaxy distribution and are an essential input in the halo model framework for studying the clustering of galaxies (for a review, see Cooray and Sheth 2002).

The results for the small box are shown in Fig. 29. For  $r \geq 0.6 \text{ Mpc}$  the deviations of the codes from the GADGET result are smaller than 10%; for  $r \geq 1 \text{ Mpc}$  the agreement is better than 5%. The FLASH result here is slightly worse because of the systematic undercounting of halos above the mass threshold of  $2 \cdot 10^{11} M_{\odot}$ . The results for the large box, shown in Fig. 30, are very similar. For  $r \geq 3 \text{ Mpc}$  the agreement of the codes with GADGET is again better than 5%, with the excep-

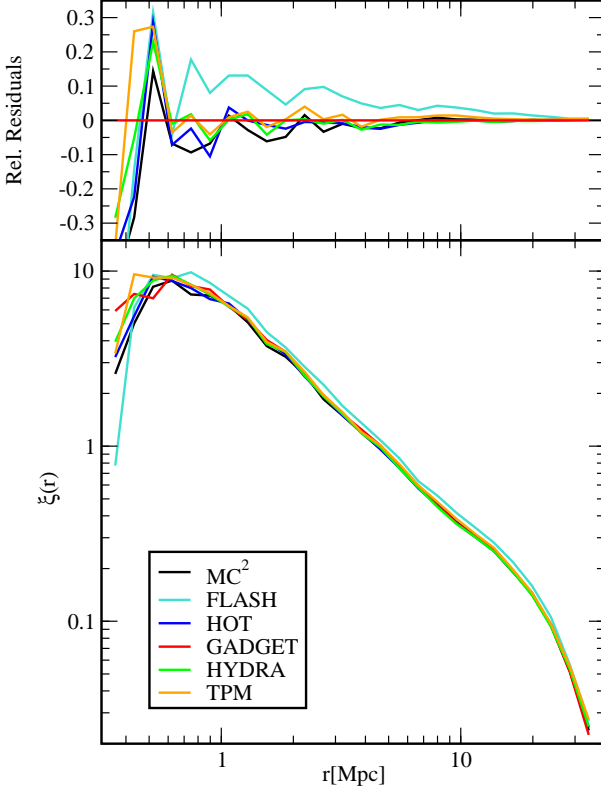


FIG. 29.— The halo two-point correlation function for the 90 Mpc box. Only halos with more than 100 particles are considered, corresponding to a threshold halo mass of  $2 \cdot 10^{11} M_{\odot}$ .

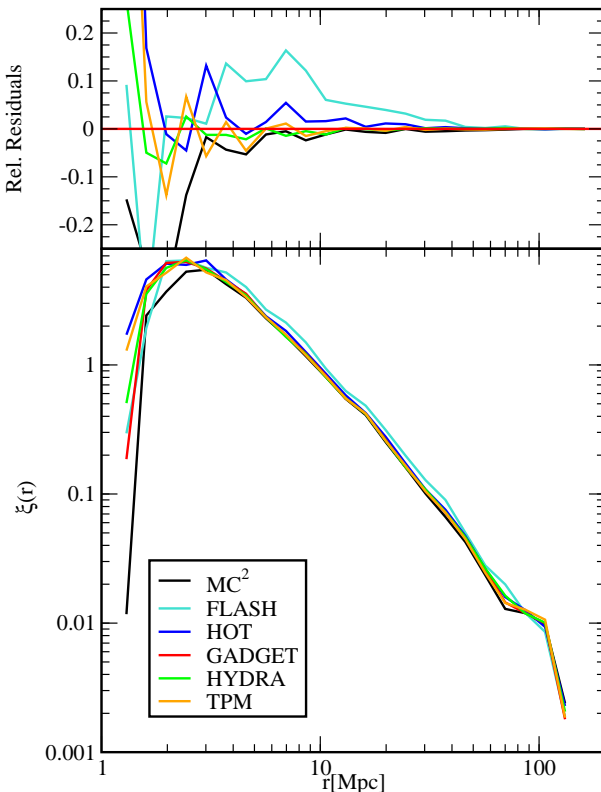


FIG. 30.— The halo two-point correlation function following Fig. 29 for the 360 Mpc box. In this case the lower halo mass cutoff is  $1.2 \cdot 10^{13} M_{\odot}$ .

tion of FLASH which disagrees over most of the range at about 10% (for the same reason as earlier). The dips in  $\xi(r)$  at the largest values of  $r$  in both boxes is a finite volume artifact, while the suppression at the smallest values of  $r$  is largely due to the length scale corresponding to the halo mass cutoffs in the two cases, approximately 0.1–0.2 Mpc for the small box and 0.5–1 Mpc for the large box. One expects the two-point function results to lose the suppression on length scales at roughly twice these values, and the simulation results are consistent with this expectation.

### 5.3.2. Halo Velocity Statistics

The single-point halo velocity statistics for the individual halos were computed using the more aggressive definition of 10 particles per halo, while the calculations of  $v_{12}(r)$  and  $\sigma_{12}(r)$  used halos with at least 100 particles as described above. To facilitate direct comparison, the individual velocity distributions were normalized by dividing by the total number of halos for each simulation.

In Fig. 31 we present the halo velocity distribution for the small box. Aside from the skewed distribution from the FLASH results due to the missing lower-mass halos, all the other codes are in reasonably good agreement. We have defined the velocity of a halo as the average velocity taken over all the constituent particles; consequently, there is an inherent statistical scatter in the comparison of the results. Light halos will have a large velocity scatter, and as light halos contribute over the entire range of velocities, this will lead to scatter in the comparative results. (Note that in this analysis we are accepting halos with only 10 particles.) The larger the halo mass, the less the scatter. Furthermore, heavier halos tend to have lower velocities and this trend is easy to spot in the better agreement below and around the peak of the distribution in Fig. 31. Up to 750 km/s the agreement is at the  $\pm 10\%$  level.

Another perspective, less sensitive to halo finder vagaries, will appear in the later analysis of direct comparisons of individual halos, given below. For halos with more than 30 particles which are simultaneously identified in the results from all the codes, the velocity scatter in the small box is approximately  $\sim 10$  km/s or less, with a corresponding value of  $\sim 20$  km/s for the larger box. As halos get heavier, there are often individual cases with relatively significant mass variation due to the FOF halo finder, and, as expected for these halos, the velocity can then show less agreement. Nevertheless, for the halos that are simultaneously found by the FOF finder in all the codes, the velocity agreement is impressive, better than a few percent.

The relative pairwise velocity for the halos and the corresponding dispersion is shown for the small and large boxes in Figs. 33 and 34. These results should be compared with the corresponding data from the individual particle analysis (Figs. 18 and 19). The points to note are that, as is well-known,  $v_{12}(r)$  is relatively insensitive as to whether particles or halos are considered, whereas this is not true of  $\sigma_{12}(r)$ , which is significantly lower for the halos.

Because of the halo sizes corresponding to the lower mass cutoffs, the smallest pair-distance scale at which the small box results should begin to make sense is  $r \sim 0.5$  Mpc, with a corresponding condition,  $r \sim 2$  Mpc for the larger box. As an inspection of Figs. 33 and 34 demonstrates, it is only after these conditions are satisfied that the code results converge, as to be expected. The results from the large box are substantially better than the results from the small box. This is because the halos

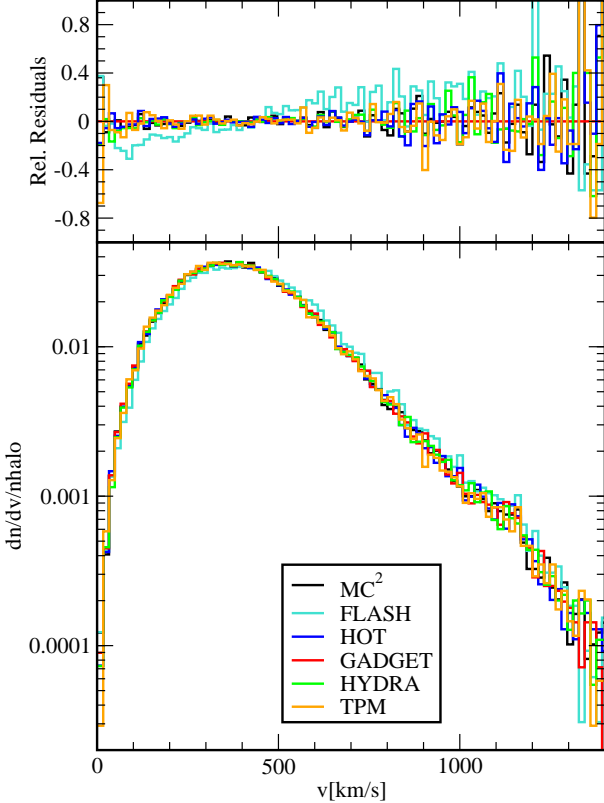


FIG. 31.— Comparison of the halo velocity distribution for all six codes at  $z = 0$ , 90 Mpc box.

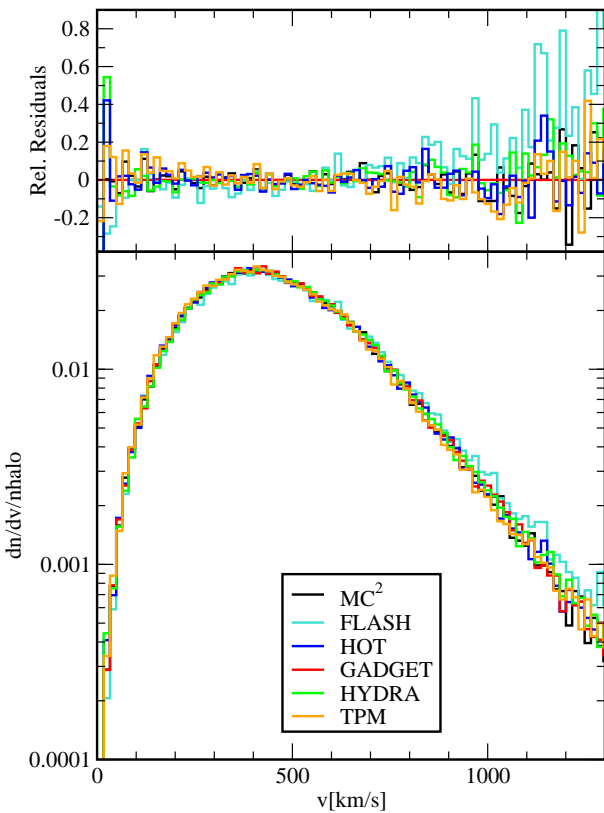


FIG. 32.— Comparison of the halo velocity distribution for all six codes at  $z = 0$ , 360 Mpc box.

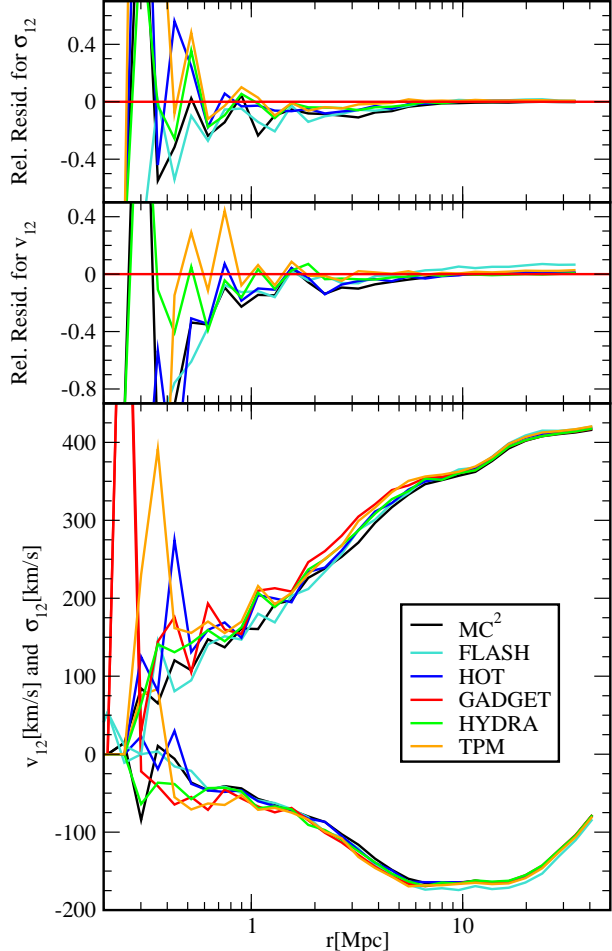


FIG. 33.— Relative mean pairwise velocity  $v_{12}(r)$  (lower set of curves) and the velocity dispersion  $\sigma_{12}(r)$  (upper set) from halos with more than 100 particles ( $M_{halo} > 2 \cdot 10^{11} M_{\odot}$ ) for the 90 Mpc box.

here have much larger masses (by a factor of 60) and are taking part in a smoother regime of the flow. Beyond  $r \sim 2$  Mpc, the codes give consistent results at the 5% level for  $\sigma_{12}(r)$ , and, except for FLASH, also for  $v_{12}(r)$ . For the lower mass halos in the smaller box, the situation is not as good. At the lower end of the acceptable  $r$  range, the error for both quantities is  $\sim 20\%$ , improving to better than 5% at a separation of a few Mpc. From the point of view of comparison to observations this is still quite acceptable, as present observational results have far worse errors and statistics limitations (Feldman et al. 2003).

### 5.3.3. Direct Comparison of Positions, Masses, and Velocities of Individual Halos

In this section we analyze and compare results for positions, masses, and velocities for specific halos directly. In contrast to the individual particles – for which such an exercise would make little sense in higher density regions – halos may be considered, in an informal sense, to be the fundamental stable mass units of cosmological N-body simulations. Thus, to the extent that this is true, we not only expect codes to agree on halo statistics but also on individual halo properties such as the individual halo masses, positions, and velocities, as well as individual halo statistics describing the internal structure of the halos. This last part has already been considered in our study of the Santa Barbara cluster where the box size and mass resolution are roughly

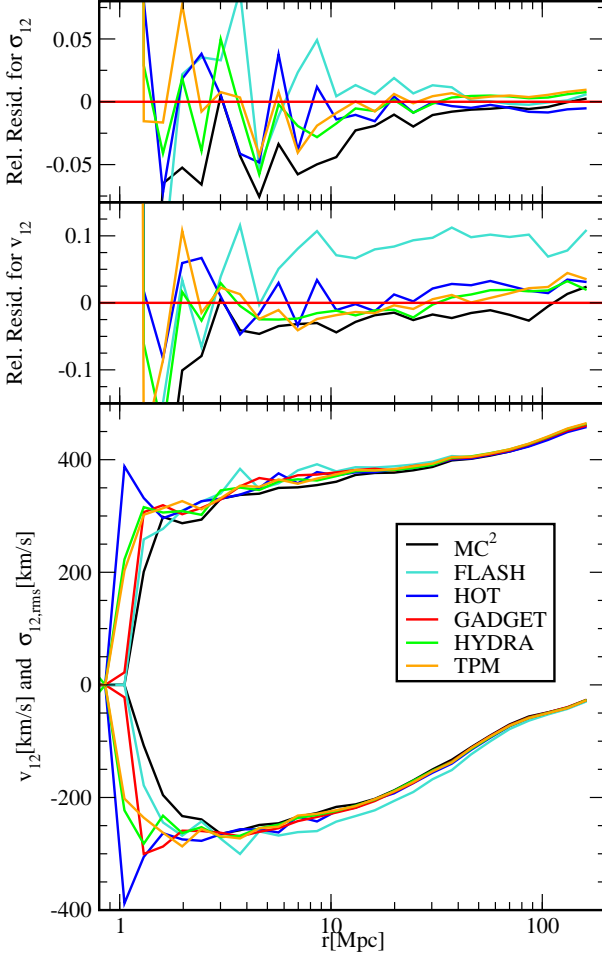


FIG. 34.— Results from the 360 Mpc box following Fig. 33. The lower halo mass cutoff here is  $1.2 \cdot 10^{13} M_{\odot}$ .

similar to the small box  $\Lambda$ CDM simulation.

We have chosen three different mass bins selecting in turn the very heaviest halos from the simulations, medium sized halos, and small mass halos in such a way that every mass bin contains roughly 40 halos. For the lighter mass bins we also employ a spatial cut, i.e., restrict ourselves to only a fraction of the simulation volume in order to keep the numbers of halos manageable. Details of the chosen cuts are given below.

First we investigate the heaviest halos in the small box. We identify all halos above a mass of  $5 \cdot 10^{13} M_{\odot}$  which corresponds to 25000 particles per halo. By imposing this mass bound we find between 38 and 39 halos in the six different simulations. Next we compare the position for every single halo. The center of each halo as defined as the particle with the largest number of friends (and thus the highest density smoothed over the scale of the linking length). We allow for a discrepancy of 0.5% in the position (which translates to 0.5 Mpc) in  $x$ ,  $y$ , and  $z$  directions for identifying the same halo in all six simulations. In Fig. 35 we show the halos found in this way with a black star. (All halos are projected onto the  $xy$ -plane.) Among the roughly 39 halos found in every simulation, 36 halos (92%) were effectively at the same position in all six simulations. In addition, we also display the halos which are *not* found in every simulation.

Next, for the halos which are identified to be at the same position in all simulations, we compute the average mass and velocity and label every halo with a labeling index. Fig. 36

shows the average mass at each index and Fig. 37 shows the average velocity at each index. In addition, we have calculated the deviation of every halo mass and velocity from the overall average:  $\delta_{m_i} = |m_i - \langle m \rangle|$  and  $\delta_{v_i} = |v_i - \langle v \rangle|$ ,  $i = 1, \dots$ . The average of these deviations:  $\frac{1}{6} \sum_{j=1,6} \delta_{m_j}$  and  $\frac{1}{6} \sum_{j=1,6} \delta_{v_j}$  describing the scatter from the average are displayed as error bars; if no error bar is present the error bar is smaller than the symbol itself; we find that the scatter for most halos is smaller than 2% for masses and velocities. The agreement in masses and in velocities is excellent; the only error bars distinguishable from the symbols are still much smaller than the naive expected statistical scatter.

The medium mass halos are analyzed in the same way. The mass slice in this case is chosen to be between  $3 \cdot 10^{12} M_{\odot}$  and  $2 \cdot 10^{13} M_{\odot}$  which corresponds to roughly 1500 to 10000 particles. In order to obtain roughly 40 halos, a spatial cut is necessary. The region analyzed in this case is a 10 Mpc slice in  $z$  from  $z = 40$  Mpc to  $z = 50$  Mpc. In Fig. 38 the identical halos from all six simulations are marked by black stars and all additionally found halos from all codes are shown. In this mass bin, 26 out of 39 halos (66%) are at the same positions in all six codes. As carried out for the heaviest halos, we calculate the average mass and velocity for each of the 26 identified halos and measure the scatter. The results are shown in Figs. 39 and 40. If no errorbar is shown, the scatter in mass and velocity is for most halos again below 2%. The masses agree very well, and only two halos show a small amount of scatter around the average. The result for the velocities is not as impressive; nevertheless, only five of the halos show significant scatter.

Finally, we analyze a subset of the lightest halos in the simulations. While our halo catalog contains halos identified at the level of 10 particles per halo, for this test we only consider halos with more than 30 particles as this is often the lowest number used in cosmological simulations. The mass range in this case is  $6 \cdot 10^{10} M_{\odot}$  to  $6 \cdot 10^{11} M_{\odot}$  which translates to 30–300 parti-

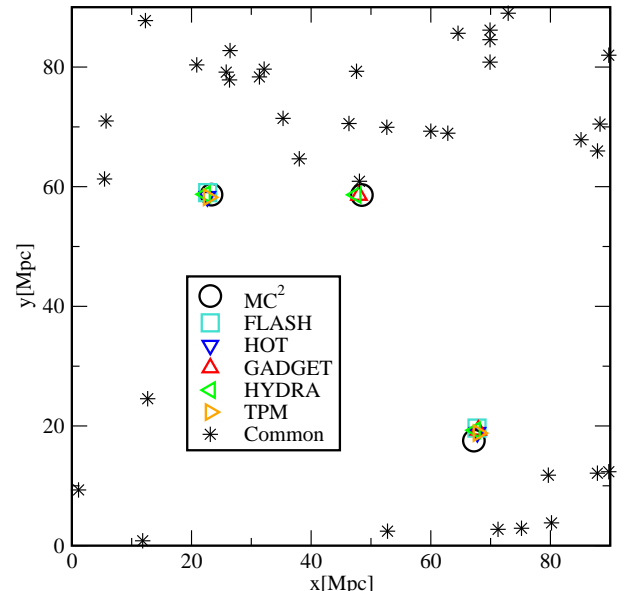


FIG. 35.— Comparison of the positions of the heaviest halos ( $M_{halo} > 5 \cdot 10^{13} M_{\odot}$ ) found in the six simulations at  $z = 0$  in the 90 Mpc box. Black stars mark halos which were found in all simulations at the same position with less than 0.5% deviation. In order to visually separate the different code symbols, the halos from the  $MC^2$  simulation were moved by 0.5 Mpc in the  $x$  direction, the HYDRA halos by -0.5 Mpc in the  $x$  direction, the FLASH halos by 0.5 Mpc in the  $y$  direction, and the TPM halos by -0.5 Mpc in the  $y$  direction.

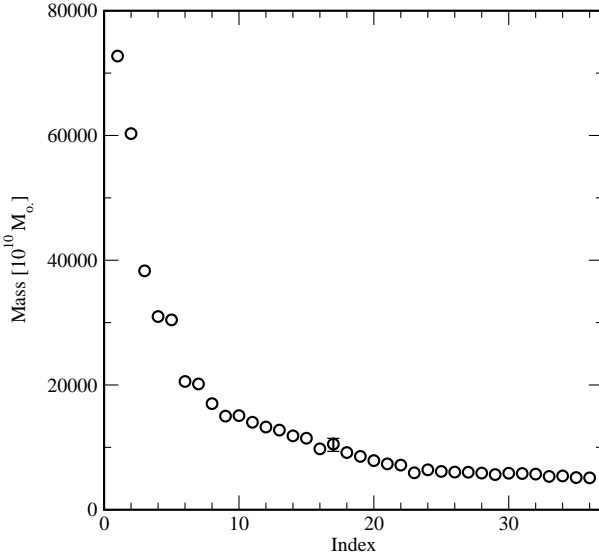


FIG. 36.— Comparison of the masses of the heaviest halos identified in all six codes at  $z = 0$ , 90 Mpc box. The  $x$  axis in the figure represents an arbitrary index label for each halo. The error bar describes the scatter of all codes from the average (see text).

cles. In addition we restrict ourselves to the inner cube between 33 Mpc and 57 Mpc in the  $x$ ,  $y$ , and  $z$  directions. Again, we identify all halos which have the same positions in the six simulations allowing for 0.5% deviation. We find 37 halos in this volume and mass bin in the different codes. In Fig. 41 we show 22 halos (60% agreement) identified in all codes at the same position with black stars and all other halos found in the simulations. The agreement in this bin is slightly worse than in the medium mass case because there are only 25 halos from the FLASH simulation. As explained earlier, FLASH produces many fewer small halos in general, therefore it is not surprising that we also find fewer small halos in a specific spatial region. Overall, the agreement is nevertheless very good. The average masses and velocities and their scatter from the 22 identified halos are shown in Figs. 42 and 43. Again, it is only for a few halos that the scatter in mass and velocity is large enough to be seen in these plots. If the scatter is not shown, it is smaller than 2%.

Overall the results of the direct halo comparison for the small box are very good. Most halos are found at identical places and with very close masses and velocities in all the simulations. (Only in the smallest mass bin were some halos lost in the lower resolution FLASH simulation.)

Next, the large box results are analyzed in a similar way. As before, we begin by considering the heaviest halos from the six simulations. All halos above a mass of  $7.32 \cdot 10^{14} M_{\odot}$  corresponding to roughly 6000 particles are considered. The heaviest halo found has a mass of almost  $2.8 \cdot 10^{15} M_{\odot}$  ( $\approx 22000$  particles). Overall 38 different halos were identified in this mass bin. From these 38 halos, 27 (71%) are at the same position in all six simulations within 0.5% corresponding to roughly 1.5 Mpc. The positions of the halos are shown in Fig. 44, black stars again showing the 27 halos found at the same position in all six codes. The halos which are not identified in all the codes are still found in most of the codes or in all the codes with a slightly larger difference in the position with only two exceptions. Remarkably, all the identified 27 halos are the 27 heaviest halos, i.e., if we would have chosen the mass cut slightly higher the

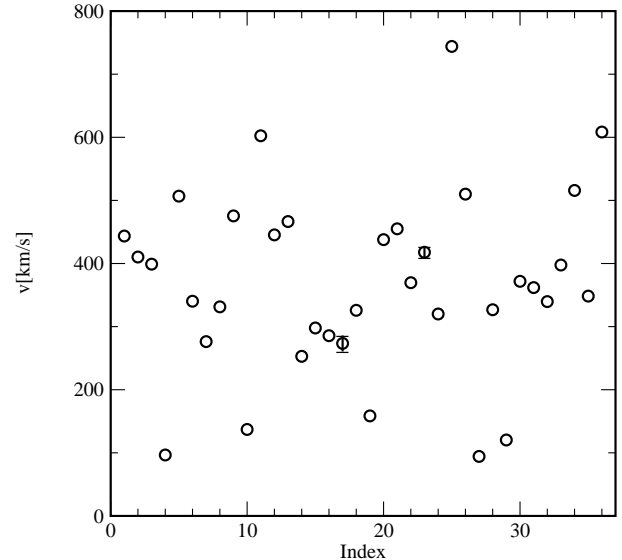


FIG. 37.— Comparison of the velocities of the heaviest halos identified in all six codes at  $z = 0$ , 90 Mpc box. The  $x$  axis shows the same index as in Fig. 36. The error bar describes the scatter of all codes from the average.

agreement would have been 100%. Next we analyze the masses and velocities of the 27 common halos, the results being shown in Figs. 46 and 47. While the scatter in mass is negligible for most halos (below 3%), halo 2, halo 3, and halo 11 show a scatter between roughly 5 to 10%, still within expected statistical errors. The mass of halo 19 varies significantly in the different simulations, with the scatter lying at 20%.

In order to understand this scatter, we have analyzed halo 19 in more detail: in Fig. 44 the red marker indicates the position of this specific halo. Halo 2 is located very close to halo 19. We show halo 19 from the  $MC^2$  simulation (which has a relatively large mass of  $1.36 \cdot 10^{15} M_{\odot}$ ) and from the GADGET simulation (with a lower mass of  $9.42 \cdot 10^{14} M_{\odot}$ ) in Fig. 45.

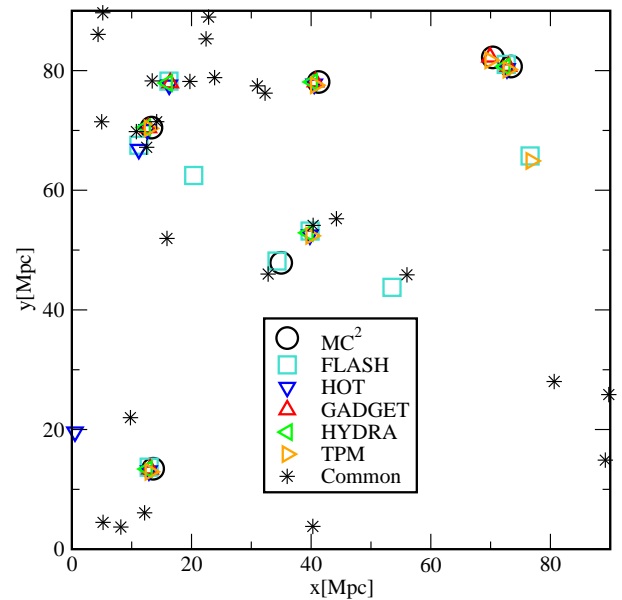


FIG. 38.— Halo positions from all six codes following the conventions of Fig. 35, but for halos containing 1500 to 10000 particles. Again, to improve visibility the halos from the different codes were shifted by  $\pm 0.5$  Mpc.

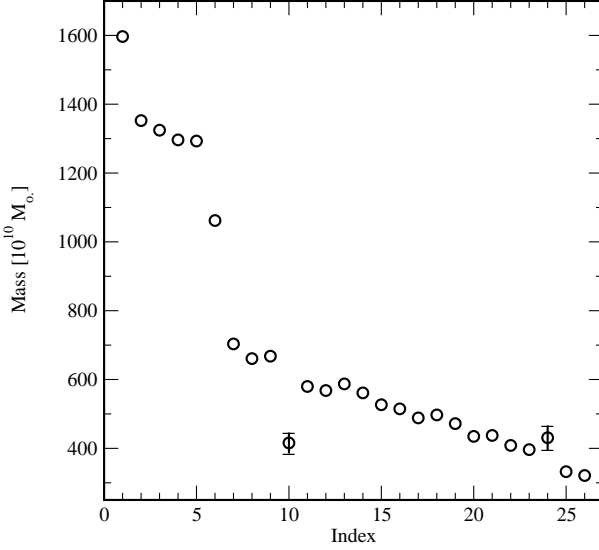


FIG. 39.—Comparison of halo masses from all six codes for halos containing 1500 to 10000 particles, 90 Mpc box.

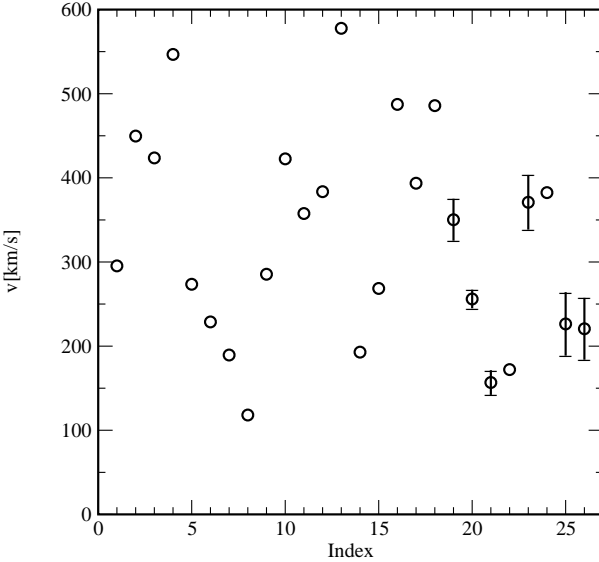


FIG. 40.—Comparison of halo velocities for halos containing 1500 to 10000 particles, 90 Mpc box.

The discrepancy is immediately clear: While in the GADGET simulation, a more or less spherical halo was found by the FOF halo finder, in the MC<sup>2</sup> simulation some particles close to the host halo built a bridge to a smaller satellite halo below the big halo. This is a well-known problem with FOF halo finders (see e.g. Gelb & Bertschinger 1994, Summers et al 1995). Due to the choice of a specific linking length, two halos which would be identified by eye as separate can be identified as being one halo if “bridging” particles between the halos are very close to each other. Spherical density algorithms are an alternative to FOF halo finders (see e.g. Lacey & Cole 1994), but this method also does not identify satellite halos separately. In the last several years, improved halo finding algorithms have appeared, especially targeted to finding subhalos in high resolution simulations. These methods are based on hierarchical FOF and bound density maxima algorithms (see e.g. Klypin et al. 1999). Since in this paper we are mainly interested in medium resolution results, a basic FOF halo finder suffices. Nevertheless, the reader

should keep in mind that results as found for halo 19 can occur with a halo finding method which is insensitive to small scale structure. Indeed, the minor code discrepancies found so far for halos could easily result from the nondefinitiveness of FOF halo-finding.

The result for the velocities (Fig. 47) is very similar to the results for the masses: six halos show significant scatter in the velocities, three of them also displaying scatter in the mass. For all six halos the scatter is around 10%, therefore below the naive statistical error. For all other halos the scatter is smaller than 3%. Overall the agreement of the heaviest halos in position, mass, and velocity is rather good.

The investigation of the medium mass halos begins by choosing a mass slice between  $3.682 \cdot 10^{14} M_{\odot}$  and  $6.137 \cdot 10^{14} M_{\odot}$  corresponding to 3000–5000 particles per halo and a spatial cut in  $z$  between 135 Mpc and 325 Mpc. Altogether 46 different halos are identified in the different simulations. MC<sup>2</sup> has 32 halos in this mass and spatial bin, FLASH has 38, HOT has 32, GADGET has the lowest number of halos in this bin with 30, HYDRA has 31, and in the TPM simulation 34 halos are found. We again ask which of these halos are at the same position if we allow for an error of 0.5% and this time find only 20 halos. In Fig. 48 these 20 halos are shown with black stars and the rest of the halos colored according to the simulation they are found in. In this mass bin, more halos are identified only in single simulations than is the case for the very heavy halos: This could be due to the fact that on the edges of the mass and spatial cuts, halos from some simulations are getting lost. Next we compare the masses and velocities of the 20 halos common to all six simulations. The results are shown in Figs. 49 and 50. The largest scatter in the mass is around 10%, still of the expected statistical fluctuation. If no errorbar is displayed, the scatter is well below 2%. More medium mass halos show a measurable scatter (half of them) than for the heaviest halos (15%). The scatter of the velocities is very small (below 2% if no errorbar is shown), the agreement of all codes being excellent. Overall, the agreement for the medium mass halos is not as good as for

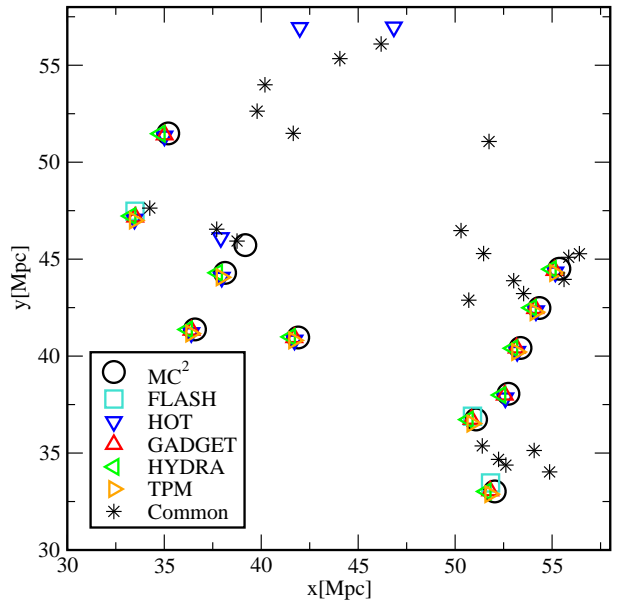


FIG. 41.—The positions of halos, following Fig. 35, for halos containing 30 to 300 particles, 90 Mpc box. In this plot, the halos from MC<sup>2</sup>, FLASH, HYDRA, and TPM were shifted by only 0.2 Mpc in the four different directions.

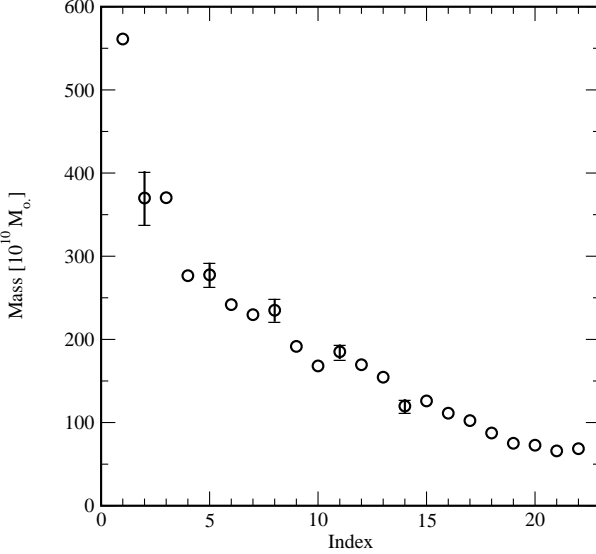


FIG. 42.— Comparison of halo masses for halos containing 30 to 300 particles, 90 Mpc box.

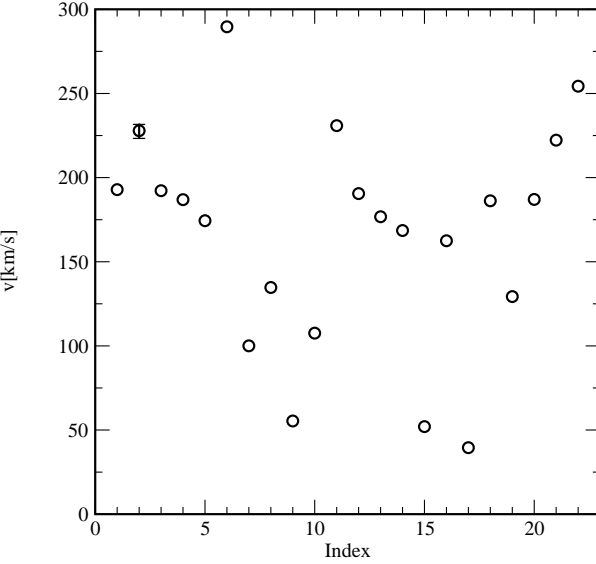


FIG. 43.— Comparison of halo velocities for halos containing 30 to 300 particles, 90 Mpc box.

the heaviest halos but still satisfactory.

The last mass range we consider consists of halos in the mass range between  $3.682 \cdot 10^{12} M_{\odot}$  and  $3.68 \cdot 10^{13} M_{\odot}$ , corresponding to 30–300 particles. We cut out an inner cube of the simulation with  $x$ ,  $y$ , and  $z$  between 158 Mpc and 202 Mpc. Overall, 43 different halos were found in all six simulations. The  $MC^2$  simulation has 25 halos in this bin, FLASH only 15, HOT 27, GADGET 35, HYDRA 33, and TPM 35. From these 43 halos, 10 are found in all simulations, again allowing for 0.5% of spatial deviation. Fig. 51 shows these 10 halos with a black star as well as all other halos. This number appears to be very small but is mainly due to the fact that the resolution of FLASH is not sufficient to resolve very small halos (as observed and discussed already for the mass function). The scatter in the masses and velocities for the 10 halos is shown in Figs. 52 and 53. The result here is very good, and all halos agree within expected statistical fluctuations.

In summary, the results for the direct halo comparison for

the large box are very consistent with our expectations. The very heavy halos show excellent agreement across all the codes, while for the very small halos the effects of force resolutions for the different codes become apparent and the results are not as good. Nevertheless, given the fact that the resolution of the two mesh codes  $MC^2$  and FLASH is an order of magnitude worse than of the other codes in these tests, the agreement for even the smallest halos is surprisingly good.

## 6. DISCUSSION AND CONCLUSIONS

In this paper we have reported the results from a detailed code comparison study with 6 codes for different test problems. For all tests the codes were given exactly the same initial conditions and the analysis of the simulation results was carried out in an identical fashion. This ensured that we only analyzed deviations arising from differences in the algorithms and their implementations in simulating the evolution of dark matter tracer particles. We restricted ourselves to medium resolution simulations, resolutions between  $\sim 10$ –100 kpc being sufficient for many applications. The codes investigated herein represented a variety of algorithms, including a plain PM-code, an AMR-code, tree-codes, a tree-PM code, and an AP<sup>3</sup>M code. Four of the codes are publicly available (FLASH, GADGET, HYDRA, TPM), and three were largely developed by us ( $MC^2$ , HOT, FLASH). We analyzed particle and halo statistics in considerable detail. All results (particle and halo catalogs) and the initial conditions are publicly available: We encourage other researchers to test their codes against our results and to devise new comparisons.

The tests employed force and mass resolutions typical of modern state-of-the-art codes used for analyzing gravitational clustering in cosmology. Overall, the results obtained are very encouraging, as the codes generally agreed to better than 5% over most of the range of interest. Larger systematic disagree-

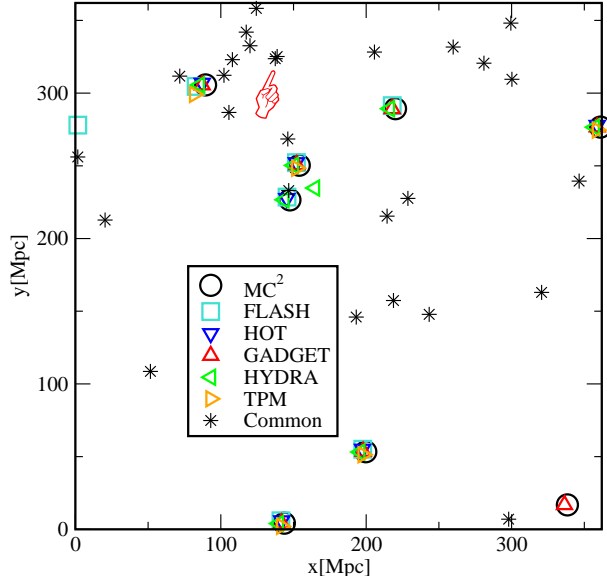


FIG. 44.— Comparison of the positions of the heaviest halos ( $M_{halo} > 7.32 \cdot 10^{14} M_{\odot}$ ) found in the six simulations at  $z = 0$  in the 360 Mpc box. Black stars mark halos which were found in all simulations at the same position with less than 0.5% deviation. To improve visibility of the code symbols, the remaining halos from  $MC^2$  had their positions shifted by 2 Mpc in  $x$ , the HYDRA halos by -2 Mpc in  $x$ , the FLASH halos by 2 Mpc in  $y$ , and the TPM halos by -2 Mpc in the  $y$  direction; the positions of the halos from GADGET and HOT were not changed.

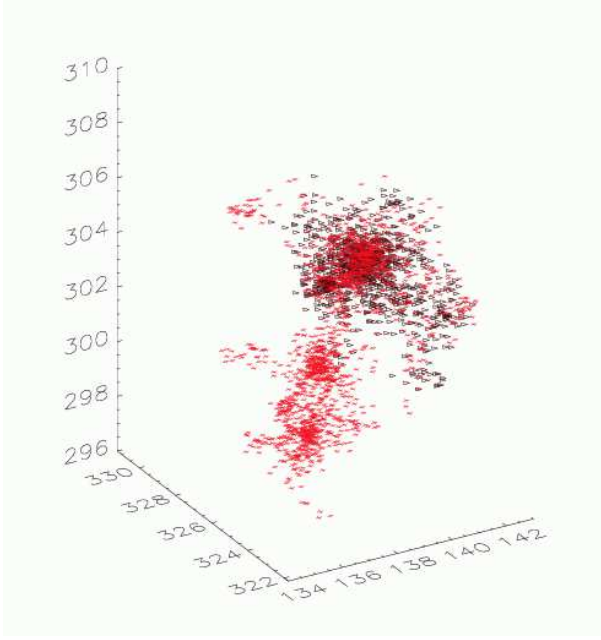


FIG. 45.— Halo 19 from the  $\text{MC}^2$  (red crosses) and GADGET simulations (black triangles). The FOF halo finder has bridged two particle “lumps” into one halo for the  $\text{MC}^2$  simulation, but not for the GADGET simulation.

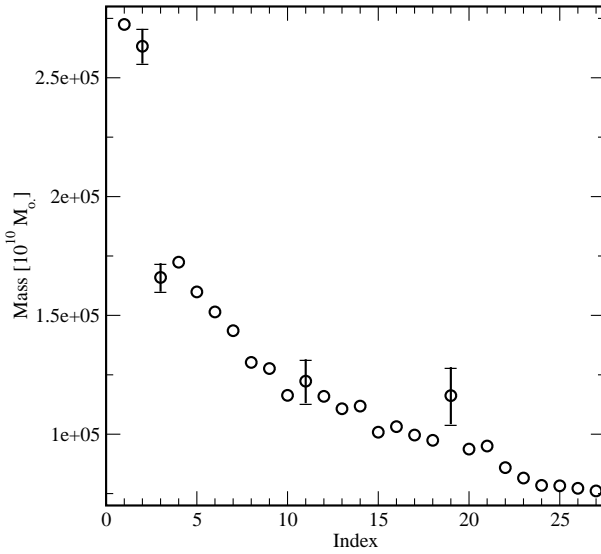


FIG. 46.— Comparison of the masses of the heaviest halos identified in all six codes at  $z = 0$ , 360 Mpc box. The  $x$  axis represents an arbitrary index label for each halo. The error bar describes the scatter of all codes from the average.

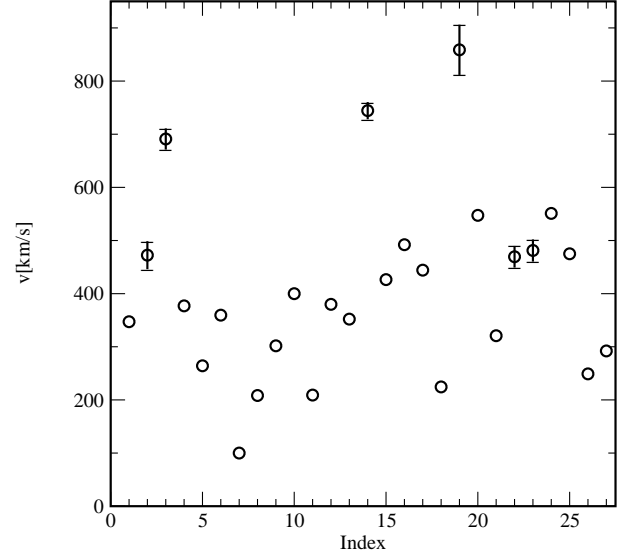


FIG. 47.— Comparison of the velocities of the heaviest halos identified in all six codes at  $z = 0$ , 360 Mpc box. The  $x$  axis shows the same index as in Fig. 46.

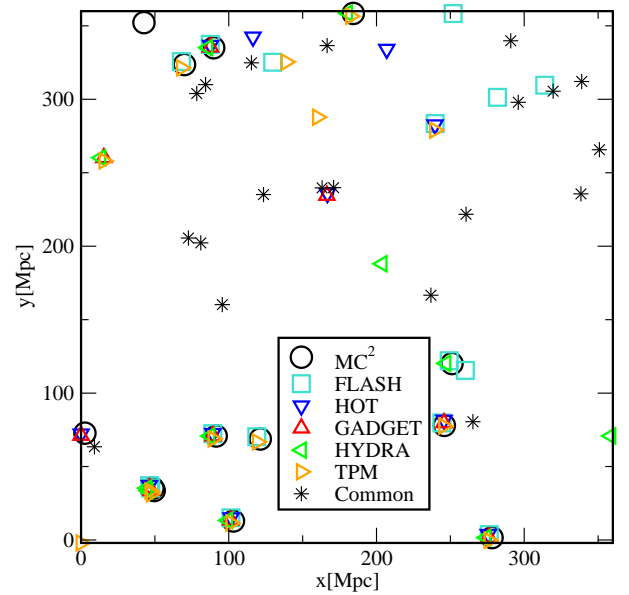


FIG. 48.— Comparison of halo positions, following Fig. 44, for halos containing 3000 to 5000 particles, 360 Mpc box. As for the largest halos, the positions of the colored halos were shifted by  $\pm 2$  Mpc to improve visibility.

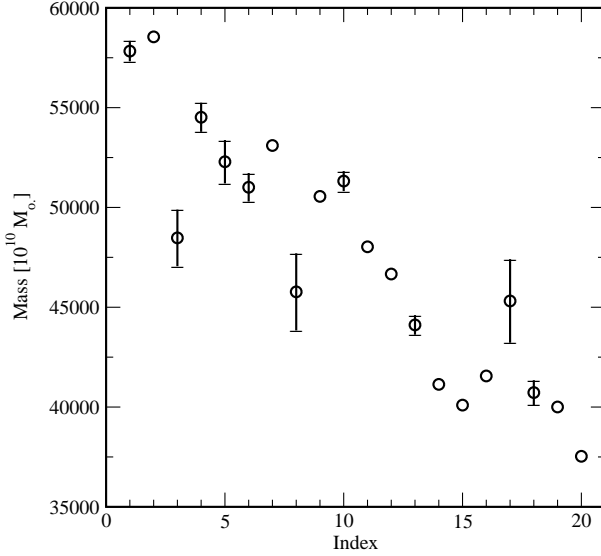


FIG. 49.— Comparison of halo masses for halos containing 3000 to 5000 particles, 360 Mpc box.

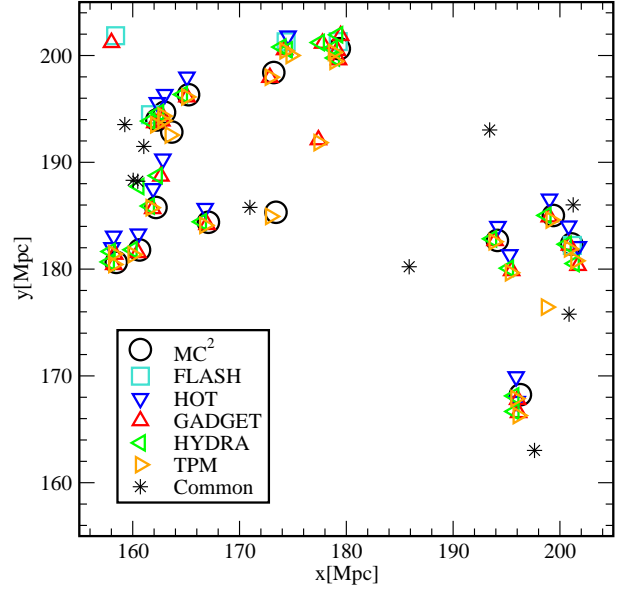


FIG. 51.— Comparison of halo positions, following Fig. 44, for halos containing 30 to 300 particles, 360 Mpc box. The code symbols were shifted by 0.3 Mpc for  $MC^2$ , FLASH, HYDRA, and TPM in the four directions to improve visibility.

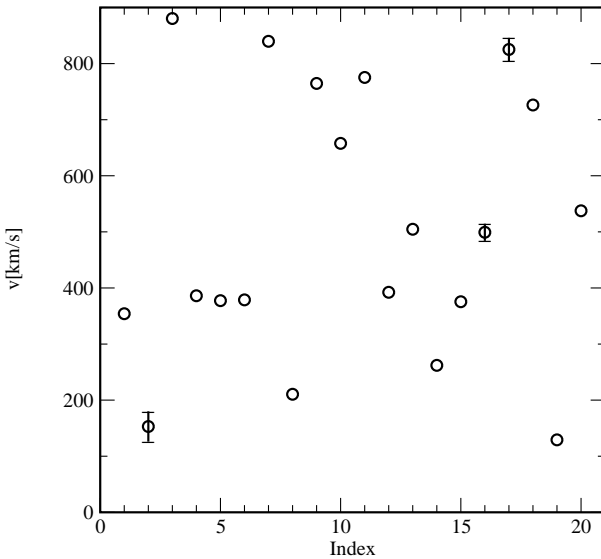


FIG. 50.— Comparison of halo velocities for halos containing 3000 to 5000 particles, 360 Mpc box.

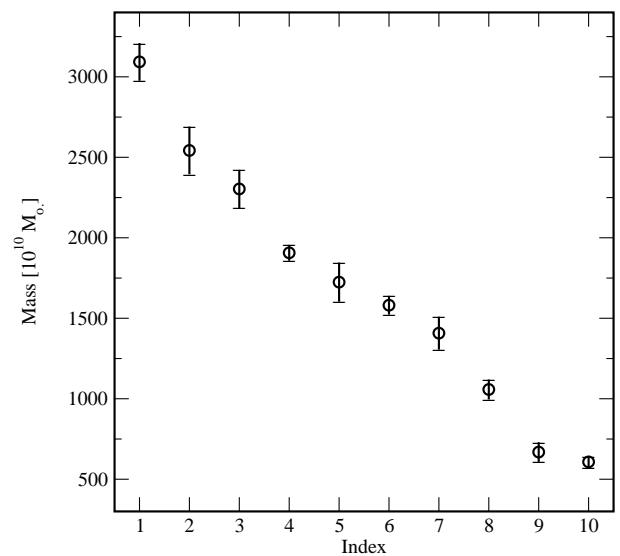


FIG. 52.— Halo masses for halos containing 30 to 300 particles.

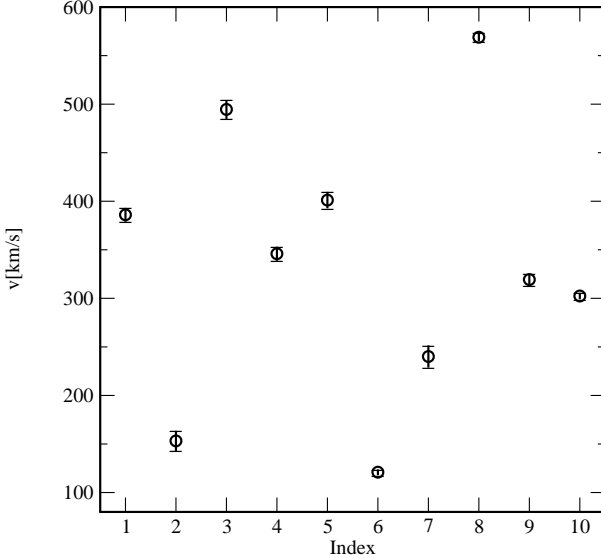


FIG. 53.— Comparison of halo velocities for halos containing 30 to 300 particles, 360 Mpc box.

ments were usually due to understandable causes such as insufficient force resolution. While the purpose of this paper is to present a broad suite of results, certain specific observations can and should be investigated in more detail, e.g., the results for the power spectrum, where the “only” 5% agreement may already provide cause for some concern.

We began our series of investigations with the Zel'dovich pancake collapse test. The PM code  $MC^2$  passed this test very easily even with relatively high force resolution while the other codes (including the AMR-code at the same force resolution) could not track the caustics forming in the nonlinear regime. We concluded that the reason for this failure is the inability of the high-resolution codes to maintain the planar symmetry of the problem and not because of unphysical collisions. Tests with cosmological initial conditions showed that the failure of the pancake test from the non-PM codes does not lead to significant errors in these more realistic situations. The excellent agreement of Richardson extrapolation-improved  $MC^2$  and GADGET results for the particle velocity distribution is also strong evidence against the presence of unphysical collisionality.

Next we investigated the dark matter component of the Santa Barbara cluster simulation running all codes with identical particle initial conditions, obtaining much better agreement between the different codes than in the original paper. Two other reasons that contributed to this were that we analyzed all simulations in the same way, and the resolution range of the simulations did not vary as much as in the original paper.

Finally, we simulated a  $\Lambda$ CDM cosmology using two boxes, one being 90 Mpc on a side, the other, 360 Mpc. Particle statistics (including velocity statistics, power spectra, and correlation functions) agreed well, the lower resolution of the mesh codes becoming apparent, as expected, in the power spectrum and the correlation functions. The agreement for halo statistics was further improved, with even the plain PM-code  $MC^2$  obtaining results very close to those from the high-resolution codes. Only FLASH and TPM deviated slightly from the other codes, for the most part with known underlying causes. The results for the halo statistics are particularly significant since

for many problems (generating mock catalogs, evolution of the halo mass function, etc.), cosmologically relevant information resides more in the spatial and mass distribution of halos and their internal structure, and less in the statistics of the underlying tracer particles.

While our findings are in general very satisfying – the codes showed almost no unexpected or unexplainable behavior and, despite the use of differing algorithms, agreed closely – in the coming age of “precision cosmology” one has to ask whether the level of agreement found here is sufficient for application to certain next-generation observations and, if not, where improvements are needed. As one example, weak gravitational lensing observations promise to deliver measurements of the mass power spectrum to an accuracy of 1%. At this level one may worry about feedback effects from baryons (White 2004, Zhan & Knox 2004) and neutrinos (Abazajian et al. 2004) as well as intrinsic code errors in modeling the distribution of dark matter (including the implementation of initial conditions, not addressed here).

As a starting point, the present agreement over a broad range of tests is gratifying, nevertheless, the lack of a rigorous quantification of error for gravitational N-body solvers is a serious barrier to future progress. As error control requirements become more severe, the need for such a theory becomes further manifest. In addition, as more (uncontrolled) physics is added, and subgrid modeling incorporated as an essential part of the simulations, it becomes ever harder to extract error-controlled results. Finally, in order to be useful, numerical results must be connected to observations. Often this can be done only indirectly and rather imprecisely, independent of the quality of the observations themselves.

Thus, to constrain the cumulative error from all links in the simulation/observation chain to less than 1%, the development of a multi-step error-control methodology is necessary. It is possible that for some applications this will remain a hopeless task, but for others it may be viable. Although the present paper in no way pretends to address the global problem, we hope that it contains useful hints for taking some of the initial steps.

S.H., K.H., and M.S.W. acknowledge support from the Department of Energy via the LDRD program of Los Alamos National Laboratory. P.M.R. acknowledges support from the University of Illinois at Urbana-Champaign and the National Center for Supercomputing Applications (NCSA). P.M.R., K.H., and S.H. acknowledge the hospitality of the Aspen Center for Physics where part of this work was carried out. The calculations described herein were performed using the computational resources of NCSA, NERSC, and Los Alamos National Laboratory. A special acknowledgement is due to supercomputing time awarded to us under the LANL Institutional Computing Initiative. Development of FLASH was supported by DOE under grant number B341495 to the Center for Astrophysical Thermonuclear Flashes at the University of Chicago. We wish to thank our many colleagues who have developed cosmological simulation and diagnostic tools and have made the tools and the results available for public use. We are indebted to Kev Abazajian, Gus Evrard, Nick Gnedin, Stefan Gottlöber, Daniel Holz, Gerard Jungman, Anatoly Klypin, Andrei Kravtsov, Adam Lidz, Zarija Lukic, Adrian Melott, Ueli Pen, James Quirk, Robert Ryne, Sergei Shandarin, Ravi Sheth, Martin White, and Yongzhong Xu for discussions and helpful advice.

## REFERENCES

Abazajian, K., Switzer, E.R., Dodelson, S., Heitmann, K., & Habib, S. 2004, astro-ph/0411552.

Anninos, W.Y. & Norman, M.L. 1994, ApJ, 429, 434.

Bardeen, J.M., Bond, J.R., Kaiser, N., & Szalay, A.S. 1986, ApJ, 304, 15.

Bertschinger, E. 1998, ARAA, 36, 599.

Birdsall, C.K. & Langdon, A.B. 1991 *Plasma Physics via Computer Simulation* (IOP).

Bode, P., Ostriker, J.P., & Xu, G. 2000, ApJS, 128, 561. <http://www.astro.princeton.edu/bode/TPM/>

Bryan, G. L. & Norman, M. L. 1997, in *Computational Astrophysics; 12th Kingston Meeting on Theoretical Astrophysics*, proceedings of meeting held in Halifax; Nova Scotia; Canada October 17 – 19; 1996, ed. D. A. Clarke & M. Fall (ASP Conference Series # 123).

Bryan, G. L. & Norman, M. L. 1999, in *Workshop on Structured Adaptive Mesh Refinement Grid Methods*, ed. N. Chrisochoides (IMA Volumes in Mathematics No. 117), 165.

Calder, A.C., et al. 2000, in *Proc. Supercomputing 2000*.

Calder, A.C., et al. 2002, ApJS, 143, 201.

Colella, P. & Woodward, P. 1984, J. Comp. Phys., 54, 174.

Colin, P., Klypin, A.A., Kravtsov, A.V. & Khokhlov, A.M. 1999, ApJ, 523, 32.

Cooray, A., & Sheth, R.K. 2002, Phys. Rep., 372, 1.

Couchman, H.M.P. 1999, J. Comp. App. Math., 109, 373.

Couchman, H.M.P., Thomas, P.A. & Pearce, F.R. 1995, ApJ, 452, 797. [http://coho.mcmaster.ca/hydra/hydra\\_consolt.html](http://coho.mcmaster.ca/hydra/hydra_consolt.html)

Davis, M., Efstathiou, G., Frenk, C.S. & White, S.D.M. 1985, ApJ, 292, 371.

Davis, M. and Peebles, P.J.E. 1977, ApJS, 34, 425.

Decyk, V.K. & Norton, C.D., <http://exodus.physics.ucla.edu/research/UPICFramework.pdf>.

Efstathiou, G., Davis, M., Frenk, C.S., & White, S.D.M. 1985, ApJS, 57, 241.

de Zeeuw, D. & Powell, K.G. 1993, JCP, 104, 56.

Feldman, H., et al. 2003, ApJ, 596, L131.

Frenk, C.S., et al. 1999, ApJ, 525, 554.

Fryer, C.L., & Warren, M.S. 2002, ApJ, 574, L65.

Fryxell, B., et al. 2000, ApJS, 131, 273. <http://flash.uchicago.edu>

Gelb, J.M. & Bertschinger, E. 1994, ApJ, 436, 467.

Habib, S., et al. 2004, in preparation.

Hockney, R.W. & Eastwood, J.W. 1989 *Computer Simulation Using Particles* (Adam Hilger, New York).

Klypin, A.A. & Shandarin, S.F. 1983, MNRAS, 204, 891.

Klypin, A.A. & Holtzman, J. 1997, astro-ph/9712217.

Klypin, A.A., Gottlöber, S., Kravtsov, A.V., & Khokhlov, A.M. 1999, ApJ, 516, 530.

Kravtsov, A.V. & Klypin, A.A. 1999, ApJ, 520, 437.

Lacey, C. & Cole, S. 1994, MNRAS, 271, 676.

Lukic, Z., et al. 2005, in preparation.

MacNeice, P., Olson, K.M., Mobarry, C., de Fainchtein, R., & Packer, C. 2000, CPC, 126, 330.

Melott, A.L. 1983, ApJ, 264, 59.

Melott, A.L., Shandarin, S.F., Splinter R.J., & Suto Y. 1997, ApJ, 479, L79.

Mo, H.J. & White, S.D.M. 1996, MNRAS, 282, 347.

Navarro, J.F., Frenk C.S., & White, S.D.M. 1995, MNRAS, 267, 401.

O'Shea, B.W., Nagamine, K., Springel, V., Hernquist, L., Norman, M.L., astro-ph/0312651.

Peebles, P.J.E. 1976a, Ap&SpS, 45, 3.

Peebles, P.J.E. 1976b, ApJ, 205, L109.

Peebles, P.J.E. 1980, *The Large-Scale Structure of the Universe* (Princeton University Press, Princeton).

Power, C., Navarro, J.F., Jenkins, A., Frenk, C.S., White, S.D.M., Springel, V., Stadel, J., & Quinn, T. 2003, MNRAS, 338, 14.

Qiang, J., Ryne, R.D., Habib, S., and Decyk, V. 2000, J. Comp. Phys., 163, 434.

Quirk, J.J. 1991, PhD thesis, Cranfield Institute of Technology.

Refregier, A., Massey, R., Rhodes, J., Ellis, R., Albert, J., Bacon, D., Bernstein, G., McKay, T., & Perlmutter, S. 2004, AJ, 127, 3102.

Ricker, P.M., et al. 2004, in preparation.

Rosner, R., et al. 2000, CiSE, 3, 22.

Ryne, R.D., Habib, S., Qiang, J., Ko, K., Li, Z., McCandless, B., Mi, W., Ng, C.-K., Saparov, M., Srinivas, V., Sun, Y., Zhan, X., Decyk, V., & Golub, G. 1998, The US DOE Grand Challenge in Computational Accelerator Physics, Proceedings LINAC98 (Chicago, IL).

Salmon, J.K. & Warren, M.S. 1994, J. Comp. Phys., 111, 136.

Sellwood, J.A. 1987, ARAA, 25, 151.

Shandarin, S., & Zeldovich, Ya.B. 1989, Rev. Mod. Phys., 61, 185.

Spergel, D.N., et al. 2003, ApJS, 148.

Springel, V., Yoshida, N., & White, S.D.M. 2001, New Astronomy, 6, 79. <http://www.mpa-garching.mpg.de/gadget/right.html>

Summers, F.J., Davis, M. & Evrard, A.E. 1995, ApJ, 454, 1.

Warren, M.S. & Salmon, J.K. 1993, in *Supercomputing '93*, 12, Los Alamitos IEEE Comp. Soc.

Warren, M.S., Fryer, C.L., & Goda, M.P. 2003, in *Proceedings of the ACM/IEEE SC2003 Conference* (ACM Press, New York).

Warren, M.S., et al. 2005, in preparation.

White, M.J., 2004, astro-ph/0405593.

Xu, G. 1995, ApJS, 98, 355.

Zel'dovich, Y.B. 1970, A&A, 5, 84.

Zhan, H. & Knox, L., 2004, astro-ph/0409198.